27764

NAME OF AUTHOR......*ALOYSIUS* *MAN-SING* *YAM*......

TITLE OF THESIS......*STIMULATED* *BRILLOUIN* *BACKSCATTERING*

OF CO_2 *LASER* *RADIATION* *FROM*

UNDERDENSE *PLASMA*

UNIVERSITY......*OF* *ALBERTA*......

DEGREE FOR WHICH THESIS WAS PRESENTED......*M. Sc.*......

YEAR THIS DEGREE GRANTED......*1976*......

Permission is hereby granted to THE NATIONAL LIBRARY

OF CANADA to microfilm this thesis and to lend or sell copies

of the film.

The author reserves other publication rights, and

neither the thesis nor extensive extracts from it may be

printed or otherwise reproduced without the author's

written permission.

(Signed)......

PERMANENT ADDRESS:

Box 1562, Regina Post Office,

Regina, Sask.

S4P-3C4

DATED......*February 6,* 19*76*

NL-91 (10-68)

THE UNIVERSITY OF ALBERTA

STIMULATED BRILLOUIN BACKSCATTERING OF CO_2 LASER RADIATION

FROM UNDERDENSE PLASMA

by

Ⓒ   ALOYSIUS MAN-SING YAM

A THESIS

SUBMITTED TO THE FACULTY OF GRADUATE STUDIES AND RESEARCH

IN PARTIAL FULFILMENT OF THE REQUIREMENTS FOR THE DEGREE

OF MASTER OF SCIENCE

DEPARTMENT OF ELECTRICAL ENGINEERING

EDMONTON ALBERTA

SPRING 1976

THE UNIVERSITY OF ALBERTA

FACULTY OF GRADUATE STUDIES AND RESEARCH

The undersigned certify that they have read,
and recommend to the Faculty of Graduate Studies and
Research, for acceptance, a thesis entitled "Stimulated
Brillouin Backscattering of CO_2 Laser Radiation from
Underdense Plasma" submitted by Aloysius Man-sing Yam
in partial fulfilment of the requirements for the degree
of Master of Science.

....
Supervisor

....
Co-Supervisor

....

....

....
External Examiner

Date ...February 6, 1976...

ABSTRACT

Wavelength resolved Brillouin backscattering of CO_2 laser radiation from underdense hydrogen and helium plasma with varying T_e/T_i ratios has been observed. The measured shift of the backscattered radiation confirms ion-acoustic waves as being responsible for such backscattering; comparison of shifts in hydrogen and helium plasmas also shows the $\sqrt{m_i}$ mass dependence expected from the Brillouin backscattering component. The experimental maximum growth rate was found to be 5.93×10^{11} sec^{-1} which agrees with the theoretical value evaluated from Tsytovich's random phase wave scattering theory. Temporal characteristics of the backscattered signal, reflectivity of the incident radiation, and pressure dependence are discussed. Experimental plasma and laser parameters also satisfied the threshold and growth rate conditions predicted by the coherent wave concept.

ACKNOWLEDGEMENT

TABLE OF CONTENTS

LIST OF TABLES

LIST OF ILLUSTRATIONS

CHAPTER I

INTRODUCTION

The concept of using a high intensity CO_2 laser beam to heat a plasma to thermonuclear temperature inside an initially uniform solenoid magnetic field was suggested by Dawson, Hertzberg and Kidder.[1] Since then, investigations related to this concept have been concerned with problems of initial generation of a plasma column which could provide a suitable density profile for self-focusing and hence trapping of the laser beam over long paths. This requires a density minimum on axis and radial confinement of the laser heated plasma by magnetic fields in the several hundred kilogauss range. In addition to normal collisional heating, consider- able interest has been shown in the study of nonlinear laser plasma interaction which could either enhance heating or alternatively lead to stimulated backscattering of the incident laser radiation.

Over the past few years, theory[2-5] and experiment[6-8] have been pursued to investigate nonlinear absorption via parametric instabilities which may lead to heating of laboratory plasmas. However, unlike the absorptive parametric instabilities which appeared to be just what was needed for fusion, stimulated scattering does relatively little plasma heating. In particular, stimulated Brillouin backscattering occurs when an incident electromagnetic wave above a certain power level is transformed via nonlinear interaction with

1

plasma into a backscattered electromagnetic wave and an ion-acoustic wave. Since this process can take place in under-dense plasma, it may lead to enhanced reflection of the incident laser beam in both the laser pellet compression and laser heated solenoid approaches to fusion, preventing efficient heating of the plasma.[9] Hence the study of stimulated backscattering may answer some questions which arise in laser-pellet fusion[10] and laser-heated solenoids.

1.1 Review of Some Work Done on Stimulated Brillouin Backscattering

(1) Theoretical

Perkins and Flick[11] have discussed the decay of an electromagnetic wave into other waves in a plasma. It was pointed out that plasma-inhomogeneities could also stabilize parametric instabilities by destroying the matching conditions between wavenumbers and frequencies.

Following this, Rosenbluth[12] gave the threshold conditions of any decay-type parametric instability (including Brillouin backscattering) in an inhomogeneous dissipationless unbounded plasma. According to his results, only spatial amplification could occur in inhomogeneous plasma, so that the threshold depended on both inhomogeneity and the size of the unstable region.

In line with the above discussion, Rosenbluth et al[13] showed the frequency shift of the ion-acoustic wave was mainly caused by inhomogeneous Doppler effect when the

plasma corona expanded with supersonic blowoff velocity.
This could be more important than the electron temperature
inhomogeneity. Also the reflectivity of the plasma and
hence the growth rate was shown directly proportional to
the intensity of the incoming wave.

Subsequently the Los Alamos group presented both
analytic theory and inhomogeneous plasma computer-simulations[14]
to show the nonlinear development of the Brillouin back-
scattering instability. Using a one-dimensional model
they verified Rosenbluth's threshold and predicted back-
scattering of the order of the incident laser energy, with
provision that particle trapping and heating effects could
significantly reduce backscattering.

Shortly afterwards, Liu and Rosenbluth[15] analysed the
growth rate and phase shift of the ion-acoustic wave and
concluded they were dependent on temperature, density and
velocity gradient of the plasma. They claimed the depletion
of pump energy undoubtedly limited the penetration depth
of the laser into the plasma. At the same time, Pesme et
al[16] gave the instability condition of stimulated Brillouin
backscattering taking all possible cases of damping, bounded-
ness and inhomogeneity into account.

Later, Shukla, Yu et al[17] published a paper on the
threshold and growth rate of the ion-acoustic wave in
Brillouin backscattering in magnetized plasmas for circularly
polarized electromagnetic waves. They found the growth rate
increased with the magnetic field for a right-hand polarized

pump wave.

(2) Experimental

Recently, stimulated Brillouin backscattering has been observed in an experiment[18] using a neodymium glass laser with peak intensity of 1.5×10^{16} watts/cm^2 and 120 psec (FWHM) pulse width, focussed on spherical targets of lithium deuteride. It was reported that the reflectivity of the plasma increased with incident intensity but saturated at a value of 10%.

At UCLA, there were reports of low level backscattering from a diffuse pinch in helium and argon.[19] The spectral shift measured using a Fabry-Perot interferometer was found in agreement with the ion-acoustic frequency shift based on an estimated plasma temperature. Thus stimulated Brillouin backscattering was indicated. Their results were poorly reproducible and they had a 0.1 to 1.5 μsec delay between backscattered signal and peak laser power. Their results perhaps require additional interpretation because the incident power to the plasma at this delay time was only 5% of the peak power of 0.4 GW.

In addition, the University of Washington group[20] measured a Brillouin backscattered signal from their under-dense magnetically confined plasma with a 300 nsec delay. At that time the incident power was about one half of their E-beam sustained CO_2 laser peak power giving a focussed intensity on the order of 10^{10} watts/cm^2. They indicated a peak reflectivity of about 0.2 to 0.5% from the plasma.

These experiments are still in progress; stimulated Brillouin backscattering will occupy the attention of both theorists and experimentalists for some time until the physics is better understood.

1.2 Nature of This Work

Despite the effort mentioned above, still little is known about stimulated Brillouin backscattering in under-dense plasma. Experimentally one would desire more information about the following: (i) the time structure of the back-scattered light, (ii) the spatial and temporal evolution of plasma during backscattering, (iii) the red-shift spectrum for different ion masses, (iv) the variation in spectra for different electron temperature to ion temperature ratio (T_e/T_i) in the presence of a plasma confining magnetic field, (v) the reflectivity dependence on incident power, and (vi) the effect of plasma density (hence the backfilling pressure of the gas before plasma is created) on backscattering.

The work reported in this thesis deals with the nonlinear interaction of a high intensity CO_2 laser beam $(\geq 10^{11}$ watts/cm$^2)$ with hydrogen and helium underdense plasma. In particular, detailed observations of stimulated Brillouin backscattering were undertaken.

In Chapter II, details of backscattering including threshold, growth rate and wave interaction related to this experiment will be discussed.

In Chapter III, the experimental apparatus and set up

will be described. This includes the high intensity laser, underdense plasma generation, red-shift spectral measurement, laser beam attenuation, magnetic field generation, optical arrangement and the timing sequence as well as synchronization.

Experimental results are described in Chapter IV. The exponential dependence of backscattered signal on incident laser power, pulse shape of signal and its dependence on backfilling gas pressure, streak photos of plasma column generation, results with and without magnetic field, reflectivity and ion mass dependence will all be presented.

A general discussion of these experimental results is given in Chapter V. The resolved red-shift spectrum confirms the ion-acoustic waves as responsible for the scattering. The qualitative difference in spectra with and without B field will be discussed. Finally, results of this experiment are compared with those previously reported by other groups.

CHAPTER II

THEORY

During the past few years, parametric instabilities and backscattering have been actively studied and theoretical predictions abound. The profusion of theories make it very hard for "an experimentalist to gain an intuitive grasp of the important physical mechanisms involved."[21] Notwithstanding all the difficult theories, one can still find two basic approaches which complement each other; one using a coherent wave concept and the other assuming a random phase wave picture. The wave concept derived by Nishikawa[22], Lashmore - Davies[23], Galeev[24] etc. used the coupled mode approach and ponderomotive force to explain parametic phenomena. In the following sections, only basic background concepts and conclusions relevant to this experiment will be quoted. One point worth noting here is that in an experiment of this sort, plasma turbulence is unavoidable. Added to this problem is the uncertainty of coherence and randomness of the back-scattered light. The best one can do is to analyse the results and determine whether they are consistent with the theories developed under the coherent wave theory and/or the random phase quantized theory.

2.1 Coherent Wave Concept

(1) Nonlinear Scattering and Interaction Mechanisms
    Nonlinear effects can be understood relatively straight-

forwardly from a physical viewpoint. In the absence of an external field, only particle thermal motion can give rise to charge separation. The self-consistent internal field given by Poisson's equation can be analyzed as non-radiating wave-like phenomena.

When an external field of sufficiently high amplitude is present, however, nonlinear effects can arise through: (i) induced inhomogeneous polarization effects created by the field acting on plasma charges and (ii) the Lorentz force term which is of order $\frac{v}{c}E$, where $v \sim \frac{eE}{m}$ thus giving rise to E^2 terms.

These mechanisms generate the interesting nonlinearities for absorption and scattering.

(2) Stimulated Brillouin Backscattering

In parametric instabilities, when an intense electromagnetic field exceeding some threshold is focussed into a plasma it can cause the growth of other waves out of the background thermal noise. These waves grow at the expense of the driving electromagnetic wave which is usually referred to as the "pump" wave. In the case of stimulated Brillouin backscattering, it is the decay of a transverse wave into another transverse wave and an ion-acoustic wave.

(i) Ion-acoustic wave

The laser irradiation induces strong particle motion. Electrons are pulled along with ions and tend to shield out electric fields arising from the bunching of ions. However,

this shielding is not perfect due to electron thermal motion. The ions form regions of compression and rarefaction, just as in ordinary sound waves. The compressed regions tend to expand into the rarefactions for two reasons: first, the ion thermal motions spread out the ions and second, the ion bunches are positively charged and tend to disperse because of the repelling electric field. This field is largely shielded out by electrons and so only a small fraction proportional to χT_e (where χ = Boltzmann's constant and T_e = electron temperature) is available to act on the ion bunches. These two effects can account for the dispersion relation[25] for ion acoustic wave which is approximately given by

$$\frac{\omega_i}{k_i} \equiv c_s \simeq (\frac{\gamma_e \chi T_e + \gamma_i \chi T_i}{m_i})^{\frac{1}{2}}$$

where

ω_i = ion acoustic frequency

k_i = ion wave number

γ = ratio of specific heats

subscript i = ion

e = electron

The electrons move rapidly relative to the wave and therefore have time to equalize their temperature everywhere. Thus they are isothermal and $\gamma_e = 1$. In motion, the ions overshoot because of their heavier mass and hence their inertia; therefore compressions and rarefactions are regenerated to form the ion-acoustic wave.

For electron temperature T_e much higher than ion temperature T_i, the dispersion equation reduces to

$$\frac{\omega_1}{k_1} = c_s \simeq \sqrt{\frac{\chi T_e}{m_i}} \qquad\qquad (1)$$

Since motion of massive ions is involved, low-frequency oscillations result.

(ii) Backscattering and Ion Contribution

The ion-acoustic waves subsequently interact with the pump laser to give another transverse wave propagating in an opposite direction to the incoming laser beam. The plasma acts as a mixer for the incident laser of frequency ω_0, wave vector k_0 and the ion-acoustic wave of frequency ω_1 and k_1. Fig. 1 shows the dispersion relation of stimulated Brillouin backscattering with ω_2 being the backscattered transverse wave. Since both ω_0 and ω_2 can be much larger than ω_p, such backscattering can occur in underdense plasma. The matching condition for ω is then $\omega_0 = \omega_1 + \omega_2$.
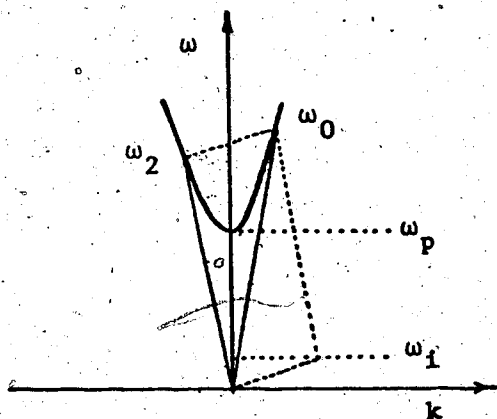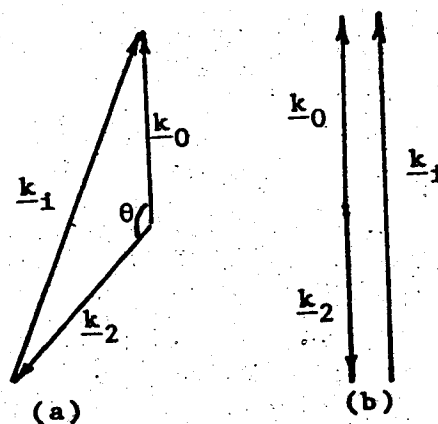
Fig 1. ω vs k Dispersion   Fig 2. Vector Wavenumber Relations

In Fig. 2(a), although the acoustic wave vector is comparable in magnitude to $\underline{k}_0$ and $\underline{k}_2$, the acoustic frequency is very small compared to the light frequency. Therefore the wave vector triangle can be considered as isosceles, with $|\underline{k}_0| \simeq |\underline{k}_2| = |k|$, hence

$$|\underline{k}_i| = 2|\underline{k}| \sin\frac{\theta}{2} .$$

The maximum acoustic frequency that can be involved in Brillouin scattering is obtained from backward scattered light, i.e. $\theta = \pi$. Since $\underline{k}_2$ is in the opposite direction of $\underline{k}_i$ and $|\underline{k}_2| \simeq |\underline{k}_0|$, therefore

$$|\underline{k}_i| = 2k_0 \tag{2}$$

note that from (1)

$$\omega_i \simeq k_i c_s$$
$$= 2k_0 c_s . \tag{3}$$

The Vlasov and Poisson equations are solved with the external field as a driving force assuming the unperturbed velocity distributions are Maxwellian[26,27]. The effective fields acting on the particles can be expressed as[28]

$$E_{eff}{}^e = -ik\frac{\phi}{e}\left(\frac{\varepsilon_i}{1+\varepsilon_e+\varepsilon_i}\right)e^{i(\omega t - \underline{k}\cdot\underline{r})}$$

$$E_{eff}{}^i = ik\frac{\phi}{e}\left(\frac{\varepsilon_e-1}{1+\varepsilon_e+\varepsilon_i}\right)e^{i(\omega t - \underline{k}\cdot\underline{r})}$$

where Φ is the potential of the external field,

e is the particle charge

and $\epsilon = \epsilon_e + \epsilon_i - 1$ is the dielectric constant of the

plasma with $\epsilon_\alpha = 1 - \frac{\omega_{p\alpha}^2}{k^2} \int_{-\infty}^{\infty} \frac{\underline{k} \cdot \frac{\partial f}{\partial \underline{v}}}{\omega + \underline{k} \cdot \underline{v}} d\underline{v}$ and α can either

be electron or ion, f is the velocity distribution of the

particle and $\omega_{p\alpha}$ is the plasma frequency of the particle.

The power dissipated by the incoming pump wave in the

plasma is found by computing the work done by the electro-

magnetic wave on the electrons and ions in the plasma over

a period of $2\pi/\omega$ giving

$$P_{diss.} = \frac{1}{2}(\frac{k\Phi}{e})^2 (|\frac{\epsilon_i}{1+\epsilon_e+\epsilon_i}|^2 Re\sigma^e + |\frac{\epsilon_e-1}{1+\epsilon_e+\epsilon_i}|^2 Re\sigma^i). \tag{4}$$

In the case when no external pump wave is applied,

resonance occurs when $1+\epsilon_e+\epsilon_i=0$. In the presence of a high

intensity pump wave, energy can be coupled to excite one of

the natural wave modes in the plasma provided matching condition

on k and ω are satisfied. In this case, it is the ion-

acoustic mode which is of most interest. Resonance occurs

when $|1+\epsilon_e+\epsilon_i|$ is very small. It can be seen that scattering

of waves is caused by both electrons and ions, however, for

Brillouin scattering the ion contribution dominates. Thus

the second term in equation (4) will contribute most to the

Brillouin backscattering.

(iii)   Threshold and Growth Rate.

Parametric instabilities can occur at any amplitude if there is no damping, but in practice even a small amount of either collisional or Landau damping will prevent the growth unless the pump wave is sufficiently strong.   Therefore there exists a threshold condition beyond which the stimulated Brillouin backscattering can take place.   Since the plasma related to this experiment is homogeneous with a column of 0.44 cm long, the threshold and growth rate for homogeneous plasma and for finite homogeneous plasma will be examined. Such conditions were summarized by Chen and in reference 21. For homogeneous plasma, the threshold is

$$(\frac{v_0}{v_e})^2 \geq \frac{8\gamma_i \nu_{ei}}{\omega_i \omega_0} \qquad (5)$$

when v_0 = quiver velocity of the electron = $\frac{eE}{m\omega_0}$

E = incoming laser field amplitude

ω_0 = laser frequency

m = mass of electron

v_e = thermal velocity of electron = $\sqrt{\frac{\chi T_e}{m}}$

ν_{ei} = ion-electron collision rate

γ_i = damping rate of ion wave .

Significant growth of the backscattered signal requires a large number of e-foldings to be detectable. In homogeneous plasma, the growth rate γ_0 is approximately given by

$$\gamma_0 \approx \frac{1}{2} \frac{v_0}{c} \left(\frac{\omega_0}{\omega_1}\right)^{\frac{1}{2}} \omega_{pi} \qquad \qquad (6)$$

In reality, if the interaction region has limited size either because of finite plasma column length ℓ or depth of focus of the laser beam, a modified threshold condition to give detectable stimulated Brillouin backscattering results.

(a) Weakly damped case

Fig. 3 shows the spatial variation of wave intensities in a finite interaction region. $\underline{k}_0$ is the pump wave; $\underline{k}_1$ is the ion-acoustic wave growing from thermal noise; and $\underline{k}_2$ is the backscattered electromagnetic wave growing

$|E_2|^2$ $|E_1|^2$

$\underline{k}_0 \rightarrow$

$\leftarrow \underline{k}_2$ Interaction Region $\underline{k}_1 \rightarrow$
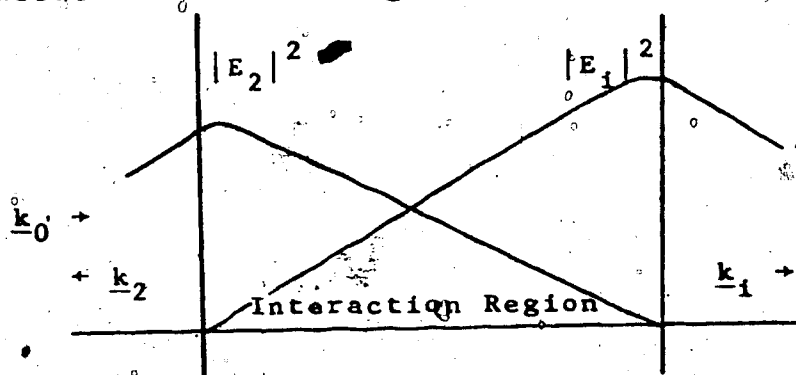
Fig. 3 Spatial Variation of Wave Intensities in a
Finite Interaction Region

essentially from zero amplitude. The growth of each wave depends on the amplitude of the other one when it exits from the region. Hence in length ℓ: the backscattered EM wave grows exponentially $\frac{\gamma_0 \ell}{c}$ times; the ion-acoustic wave grows exponentially $\frac{\gamma_0 \ell}{c_s}$ times, in which c and c_s are phase velocity of the respective wave. Since each wave is bootstraping the

other, the overall e-folding depends upon the product of

the two giving:

$$\frac{\gamma_0 \ell}{c} \cdot \frac{\gamma_0 \ell}{c_s} = \frac{\gamma_0^2 \ell^2}{c c_s}$$

To achieve substantial growth, the e-folding has to be much

greater than 1

$$\frac{\gamma_0^2 \ell^2}{c c_s} \gg 1. \tag{7}$$

Relation (7) will be true so long as the growth rate is

greater than the geometric mean of the damping rates,

i.e.

$$\gamma_0 \gg \gamma_T = \sqrt{\gamma_1 \gamma_2}$$

$$= \left(\frac{\gamma_i \nu_{ei}}{2}\right)^{\frac{1}{2}} \left(\frac{\omega_p}{\omega_0}\right). \tag{8}$$

Pesme et al[16] showed when γ_i is not small, (7) is valid

when

$$\gamma_0 \gg \gamma_c \equiv \frac{1}{2}\sqrt{v_1 v_2} \left| \frac{\Gamma_1}{v_1} - \frac{\Gamma_2}{v_2} \right|$$

or

$$= \frac{1}{2}\gamma_i \sqrt{\frac{c}{c_s}} \quad \text{in this case} \tag{9}$$

where Γ_1 and Γ_2 are linear damping rates of the two waves.
Thus when γ_0 is bounded by $\gamma_T < \gamma_0 < \gamma_c$, no absolute instability

occurs and there will not be growth without limit.

(b) Intermediate damping case

For reasonable T_e/T_i ratios, ion Landau damping is non-

negligible. The ion wave will then lose energy through

damping more rapidly than by convection out of the growth region. With the plasma column ℓ, the ion-wave exponentiates $\gamma_0 \ell / c_s$ times while being damped $\gamma_i \ell / c_s$ times resulting in an exponentiation of γ_0 / γ_i. Meanwhile, the backscattered EM wave e-folds $\dfrac{\gamma_0 \ell}{c}$ times, and the overall e-folding is

$$\frac{\gamma_0}{\gamma_i} \frac{\gamma_0 \ell}{c} = \frac{\gamma_0^2 \ell}{c \gamma_i}$$

implying $\dfrac{\gamma_0^2 \ell}{c \gamma_i} \gg 1$ (10)

is the condition for large e-folding.

2.2 Random Phase Theory

(1) Brief Description of Basic Ideas

The wave packet shown in Fig. 4 represents a set of superimposed plane monochromatic waves possessing a restricted range of wavenumbers $\underline{k}$ and hence, finite range of $\omega(\underline{k})$. It has a mean value $\underline{k}_0$, with a spread δk about this mean $\underline{k}_0$; and similarly a spread $\delta \omega$ where $\delta k \ll k_0$ and $\delta \omega \ll \omega_0$.
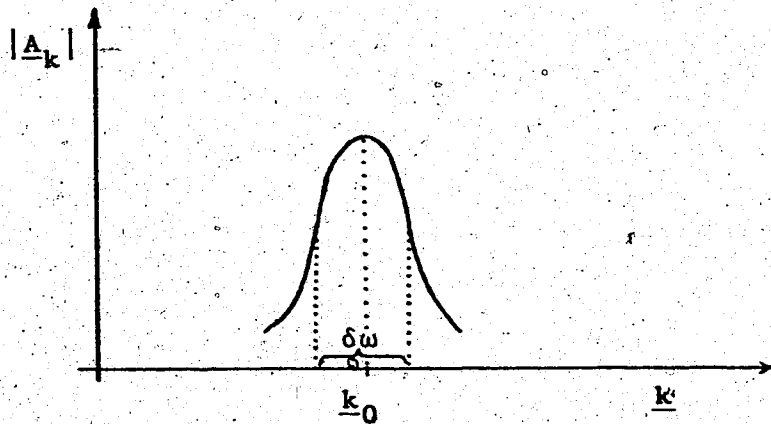
Fig. 4 Wave Packet of Mean Value Wavenumber $\underline{k}_0$

The field of the packet is represented by

$$E = \int A_k \, e^{i\omega(\underline{k})t + i\underline{k}\cdot\underline{r}} \, d\underline{k}$$

where $\underline{A}_k$ is the complex amplitude of the packet with a maximum at $\underline{k}=\underline{k}_0$. Hence $\underline{A}_k = |\underline{A}_k| e^{i\phi_k}$ where ϕ_k is the phase of the Fourier component.

When the phases of the interacting waves can be considered random, either because of a broad frequency spectrum or long interaction time such that $\phi = \Delta\omega t \gg 1$, it is essential to modify the coupled equations governing exchange of energy between modes. In such a case, it is useful to quantize the fields since only mean square amplitudes are important, i.e. pump intensity

$$<E^2> = \int |A_k|^2 d\underline{k} \; .$$

This theoretical approach has been given by Tsytovich[29] and using this quantized approach, i.e. $N_k \sim |E|^2$, it is necessary that energy and momentum of quanta be conserved, i.e.

momentum conservation $\hbar\underline{k}_0 = \hbar\underline{k}_1 + \hbar\underline{k}_2$

energy conservation $\hbar\omega_0 = \hbar\omega_1 + \hbar\omega_2$.

Thus for random phase waves, the finite bandwidth permits coupling over a range of wavenumbers and frequencies where the intensity per unit wavenumber is the important driving term. Growth will be greatest for $\underline{k}_0$ but possible for slight mismatch in frequency and wavenumber.

(2) Growth rate

Introducing the number density of photons in the wave packet as N_k, Tsytovich[30] gives an expression for the rate of scattering of photons from wavenumber $\underline{k}'$ into wavenumber $\underline{k}$ by particle α as

$$\frac{1}{N_k} \frac{dN_k}{dt} = \gamma_k \qquad (11)$$

$$= \iint \frac{d\underline{v}\,d\underline{k}'}{(2\pi)^3} \frac{\hbar(\underline{k}-\underline{k}')}{m_\alpha} \frac{\partial f^\alpha}{\partial \underline{v}} W N_{k'} \qquad (12)$$

where f^α is the velocity distribution function of particle α;

W is the probability of transfer of one particular mode into another;

$N_{k'}$ is the photon number density in $\underline{k}'$ space.

(3) Present Case

The growth rate of the backscattered transverse wave in general is determined by both ions and electrons. From Tsytovich[31], the probabilities of tt-scattering by plasma electrons and ions are respectively:

$$W_p^e = \frac{(2\pi)^3 e^4}{m_e^2 2\omega\omega'} \left[1 + \frac{(\underline{k}\cdot\underline{k}')^2}{k^2 k'^2}\right] \left|\frac{\varepsilon_i}{\varepsilon_o}\right|^2 \delta[(\omega-\omega') - (\underline{k}-\underline{k}')\cdot\underline{v}]$$

$$W_p^i = \frac{(2\pi)^3 e^4}{m_e^2 2\omega\omega'} \left[1 + \frac{(\underline{k}\cdot\underline{k}')^2}{k^2 k'^2}\right] \left|\frac{\varepsilon_e-1}{\varepsilon}\right| \delta[(\omega-\omega') - (\underline{k}-\underline{k}')\cdot\underline{v}]. \qquad (13)$$

Hence from equation (12)

$$\gamma_k = \int \frac{d\underline{v}d\underline{k}'}{(2\pi)^3} \frac{\hbar(\underline{k}-\underline{k}')}{m_i} \frac{\partial f^i}{\partial \underline{v}} W_p^{\ i} \delta[\Delta\omega - \Delta\underline{k}\cdot\underline{v}]N_{\underline{k}'}$$

$$+ \int \frac{d\underline{v}d\underline{k}'}{(2\pi)^3} \frac{\hbar(\underline{k}-\underline{k}')}{m_e} \frac{\partial f^e}{\partial \underline{v}} W_p^{\ e} \delta[\Delta\omega - \Delta\underline{k}\cdot\underline{v}]N_{\underline{k}'} .$$

Tsytovich has also shown induced scattering by ions, if allowed by conservation laws, usually exceeds scattering by electrons when $|\underline{k}-\underline{k}_0|\lambda_D << 1$ (λ_D = Debye length). Also the small $\Delta\omega$ shows ions contribute most (Equation (1)). Therefore the growth rate reduces to

$$\gamma_k = \int \frac{d\underline{v}d\underline{k}'}{(2\pi)^3} \frac{\hbar(\underline{k}-\underline{k}')}{m_i} \frac{\partial f^i}{\partial \underline{v}} W_p^{\ i} \delta[\Delta\omega - \Delta\underline{k}\cdot\underline{v}]N_{\underline{k}'} . \qquad (14)$$

The analytic and numerical integration of this equation for the present experimental conditions will be deferred to Chapter IV, where the results will be discussed both theoretically and experimentally. It can be seen from equation (14) that γ varies linearly with intensity of the incoming beam and plasma particle density. Integration of (11) gives the growth of the backscattered wave

$$N_k \propto e^{\gamma t} = e^{\gamma(I,n)\frac{\ell}{c}} \qquad (14a)$$

where ℓ is the interaction length.

2.3 Dispersion Relation

From references (25) and (31), if the electron velocity v_e satisfies $v_e \gg \frac{\omega_i}{k_i} \simeq c_s$

then
$$\varepsilon = \varepsilon_e + \varepsilon_i - 1$$

$$\simeq 1 + \alpha^2 - \frac{\omega_{pi}^2}{\omega_i^2}[1 + \frac{3k_i^2 v_i^2}{\omega_i^2} + \dots] + i\sqrt{\pi}\, x e^{-x^2}$$

where

$$\alpha^2 \equiv \frac{1}{k_i^2 \lambda_D^2} \equiv \frac{1}{k_i^2}\left(\frac{XT_e}{4\pi n e^2}\right)^{-1} \quad \text{and} \quad x = \frac{\omega_i}{\sqrt{2}k_i v_i}.$$

For small damping, resonance occurs when

$$1 + \alpha^2 = \frac{1 + k_i^2 \lambda_D^2}{k_i^2 \lambda_D^2}$$

$$= \frac{\omega_{pi}^2}{\omega_i^2}[1 + \frac{3k_i^2 v_i^2}{\omega_i^2} + \dots]$$

Approximation to first order gives,

$$\omega_i^2 \simeq \frac{\omega_{pi}^2 k_i^2 \lambda_D^2}{1 + k_i^2 \lambda_D^2} \simeq \frac{k_i^2 c_s^2}{1 + k_i^2 \lambda_D^2}$$

and to second order gives

$$\omega_i{}^2 \simeq \frac{\omega_{pi}{}^2}{1+\alpha^2} \left[1+\frac{3k_i{}^2 v_i{}^2}{\omega_i{}^2}\right]$$

$$= \frac{\omega_{pi}{}^2}{1+\alpha^2} \left[1+\frac{3v_i{}^2}{v_\phi{}^2}\right]$$

where v_ϕ is the phase velocity of the ion-acoustic wave.

For $\alpha \gg 1$

$$\omega_i{}^2 \simeq \frac{\omega_{pi}{}^2}{\alpha^2} \left[1+\frac{3v_i{}^2}{v_\phi{}^2}\right]$$

$$= k_i{}^2 c_s{}^2 \left[1+\frac{3v_i{}^2}{v_\phi{}^2}\right] \qquad (15)$$

also when v_i/v_ϕ is small, the second order approximation is sufficiently accurate to calculate the sound speed; equation (15) reduces to

$$\omega_i \simeq k_i c_s \left(1+\frac{3}{2}\frac{v_i{}^2}{v_\phi{}^2}\right) \qquad (16)$$

and v_ϕ is determined experimentally from $v_\phi = \omega_i/k_i$.

CHAPTER III

APPARATUS AND EXPERIMENTAL DETAILS

3.1 The 1GW Laser

In most of the recent reports on laser-plasma inter-
action experiments of the same nature, focussed laser inten-
sities were greater than 10^{10} watts/cm^2. The laser used in
this experiment was designed and constructed at the University
of Alberta.[32] It is a high power transversely excited
atmospheric (TEA) CO_2 laser and is U.V. preionized. This
type of laser was first reported in 1973.[33]

(1) Laser Cavity — Mechanical

In the 3 meter long laser oscillator cavity there are
6 discharge modules (Fig. 5), each having an identical
electrode configuration and electrical excitation circuitry.
The electrodes used in each module are modified Rogowski-
profiled graphite anode and aluminum cathode 50 cm long by
3.7 cm wide. The separation between the electrodes is 3.7
cm as shown in Fig. 6. Preionization is provided by a string
of eight 570 pF capacitors attached with stainless steel
pointed electrodes placed at 6 cm intervals along each side
of and electrically connected in parallel with the main
electrodes. The laser cavity is equipped with a flat gold
mirror on one end and a flat NaCl window on the other.

(2) Laser Triggering and Excitation Circuitry
(see Fig. 5)
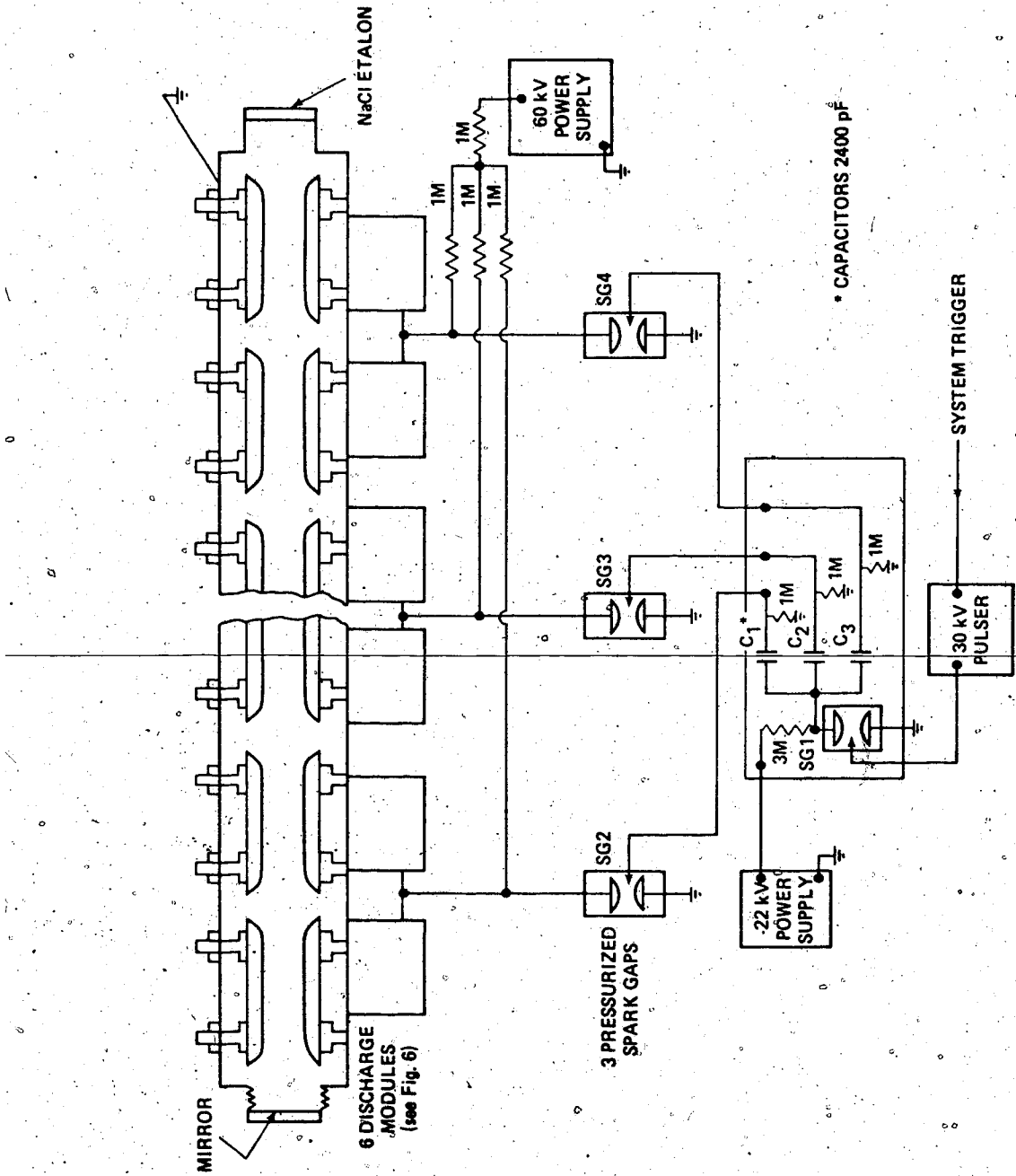
Fig. 5   Laser Triggering and Excitation Circuitry
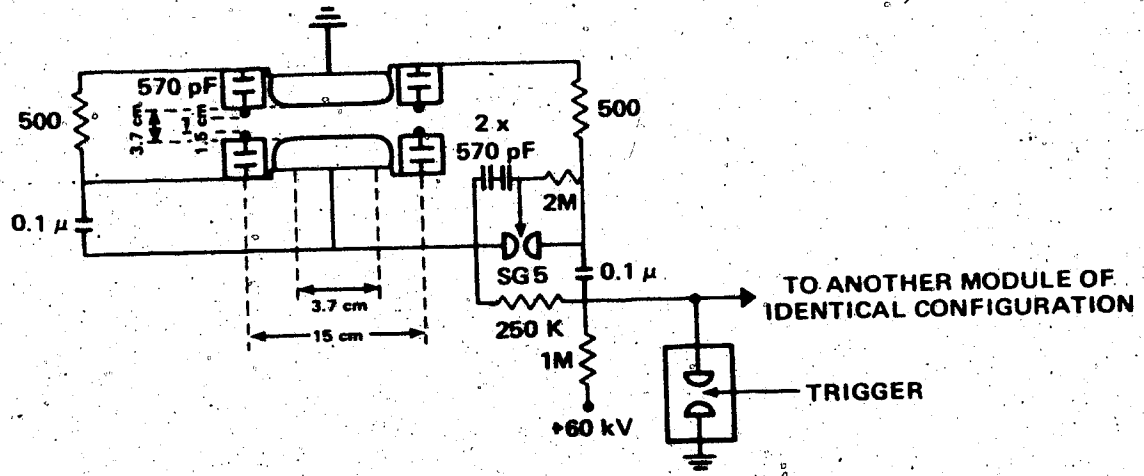
Fig. 6 . Laser Discharge Modules Configuration
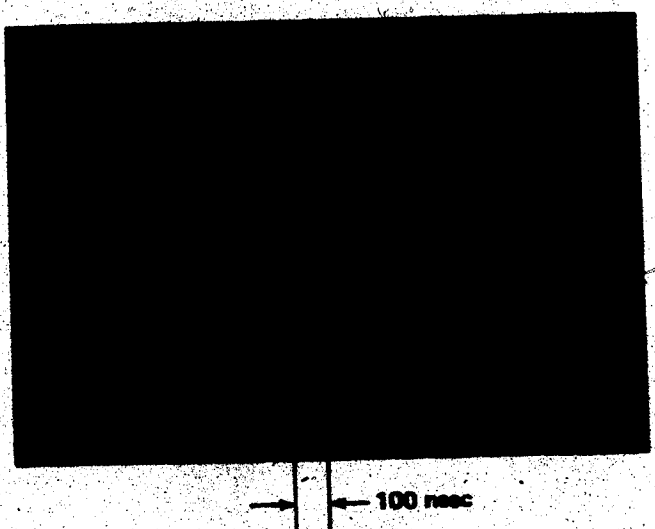
Fig. 7. Typical Laser Signal

(3)   Brief Description of Operation

While the physics of the CO_2 laser, with a mixture of CO_2, He and N_2, has been well established in the past years,[34] the use of bright arc discharges as preionizers for pulsed CO_2 lasers was first reported in 1972.[35,36,37] However, the first confirmation of the production of volumetric photo-ionization by the radiation from auxiliary arc discharges in a CO_2 laser discharge did not come until 1973. In the following, the sequence of events leading to photo-ionization of the gas in the laser cavity in this system will be briefly described. Sequence of events:[38]

(i) When a system trigger is applied to the E.G.&G. 30 KV pulser, spark gap SG1 is fired (Fig. 5). This permits charged capacitors C_1, C_2 and C_3 to provide simultaneous high voltage pulses for triggering the main spark gaps SG2, SG3 and SG4 of the laser discharge system.

(ii) Each of these spark gaps initiates discharge of two modules connected in parallel. The storage capacitors are energized by the +60 KV supply. SG5 is self-triggered and the strings of 570 pF capacitors generate high current arcs ahead of the main discharge due to shorter interelectrode distance.

(iii)High current density arcs are produced by the multiple electrodes. The gas inside the active volume is partially ionized and the onset of this photo-ionization propagates rapidly enough that it extends across the whole active region before the main discharge occurs and laser action

takes place.

(4)   Summarized Characteristics of this Laser

List	Calculated or Measured Numbers		
Number of Discharge Modules		= 6	
Active Cross-sectional Area	3.7 cm×3.7 cm	= 13.69 cm^2	
Total Active Volume	(3.7×3.7×50)×6	= 4.11 litres	
Optical Resonator Length		= 3 meters	
Optics (Mirror & Window)		= 3.5 in. Dia.	
Divergence		= 2.5 milliradians	
Gas Composition at Normal Run	CO_2 N_2 He	= 30% = 30% = 40%	
Operating voltage		= 50 KV	
Energy Storage Capacitors		= 0.1 µF, 20 nH	
Total Input Energy		= 1500 Joules	
Maximum Output Energy		≃ 125 Joules	
Maximum Output Power		≃ 1 GW	
Conversion Efficiency		= 8%	
Laser Current Pulse		= 200 nsec	
Laser Output Pulse Duration and Power (Fig. 7)	Initial Pulse Tail	= 40 nsec, 1 GW peak = 1 µsec, 200 MW peak	

Table I.   Characteristics of the Laser

MONO-CHROMATOR

FABRY-PEROT INTERFEROMETER

BAND-PASS FILTER

Ge : Au DETECTOR

SIGNAL TO OSCILLOSCOPE

ATTENUATION CELL

ALIGNMENT CO$_2$ LASER

BS

SIGNAL TO OSCILLOSCOPE

JOULE METER

BS

SIGNAL TO OSCILLOSCOPE

VACUUM TANK

SOLENOID VALVE

LENS

CO$_2$ SPECTRUM ANALYZER

GAS RESERVOIR

IRIS

COIL

C

LASER

PULSED CO$_2$

MIRROR
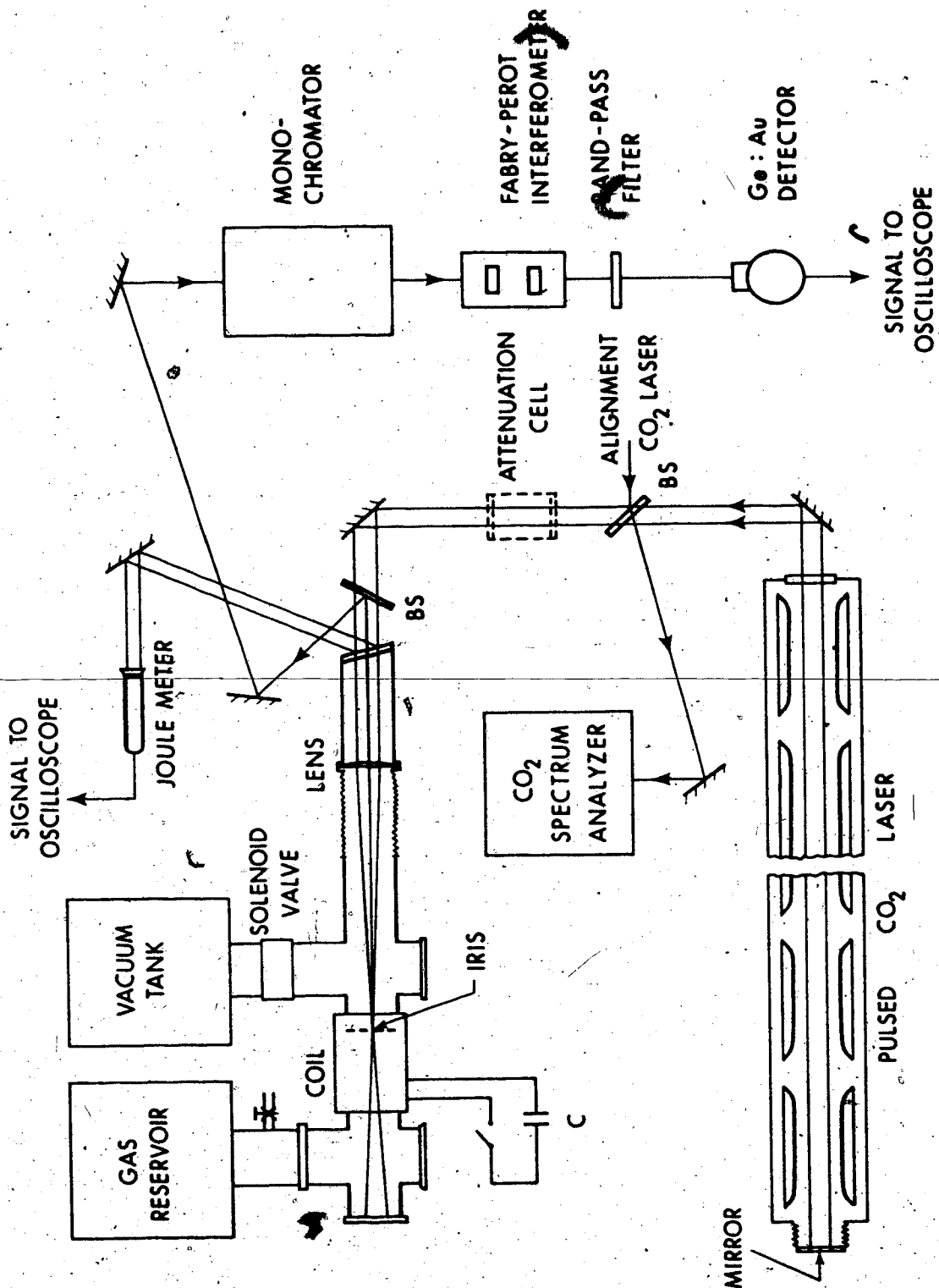
Fig. 8   Schematic Diagram of the Experimental Set-up

In the present experiment, a 52 cm focal length lens was used which gave peak focussed intensities of $\approx 10^{11}$ watts/cm^2.

3.2 General Description

(1) Setup

A schematic diagram of the experimental arrangement is shown in Fig. 8. Considerable care in optical alignment had to be exercised due to the complexity of optics involved. This alignment was achieved by using a 2 mW He-Ne laser (not shown in figure) along with a chopped CW CO_2 laser ($\leq$ 5W) to simulate the pulsed laser beam. In this way, the optical system including monochromator, Fabry-Perot interferometer and detectors could be carefully aligned. A CO_2 spectrum analyser was positioned to monitor the P20 transition of the CW CO_2 laser during alignments.

An attenuation cell was employed to control incident power to the plasma cell. The front section to which the 52 cm-focal-length lens was attached was evacuated to less than 100 microns to prevent gas breakdown by the lens re-flected and back-focussed laser beam. A 20° angled window was used to eliminate back reflection of the main beam and a beam splitter to facilitate coupling of backscattered signal to the monochromator and remaining optical system.

The purpose and description of various parts of the arrangement will be given in the following sections before the plasma diagnostic techniques are described.

3.3 Plasma Generation

The plasma cell is shown in Fig. 9 with the solenoid removed. The use of a 4.5 mm diameter iris at the focal point to permit differential pumping was critical to the underdense plasma generation. To understand why, the following phenomena during gas breakdown will be reviewed.

(1) Background Concept

The occurrence of an opaque backward going breakdown wavefront to an incident CO_2 laser during laser-supported detonation of underdense hydrogen was first observed by Burnett and Offenberger.[39,40] They observed that when a laser beam was focussed into gas with a filling pressure low enough (< 20 Torr) such that when fully ionized electron densities were below cutoff, a breakdown heating front propagated in both directions from the focal spot at near equal velocities. However, they found that if the laser intensity at the backward going front (opposite to incoming laser) decreased to a value $\leq 10^8$ watts/cm^2, it could no longer heat the backward wavefront region transparent enough to deliver energy to the forward going wavefront region to sustain plasma generation. To eliminate this backward wave in the present set-up, an orifice[40,41] was placed at the focal point to permit differential pumping of the gas in the focal cone region and hence reduce laser absorption.

(2) Iris Function

To reduce the backward going wavefront absorption in
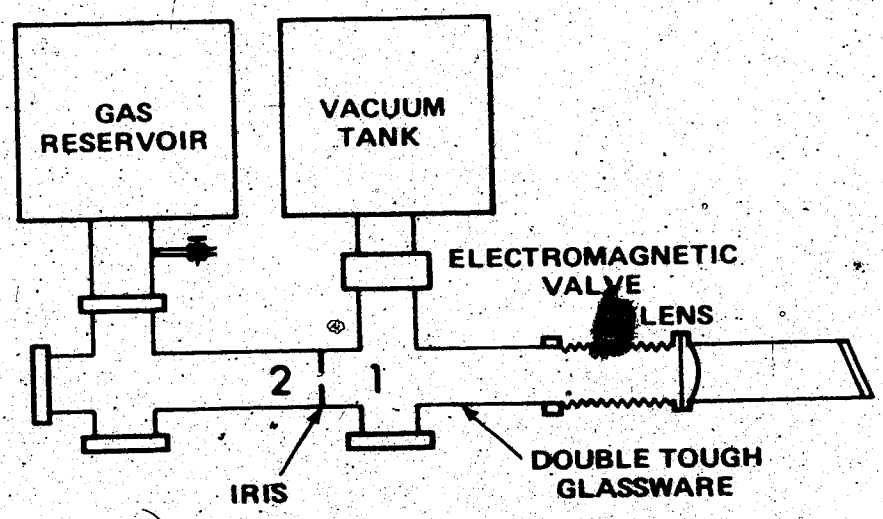
Fig. 9   Plasma Cell and Iris
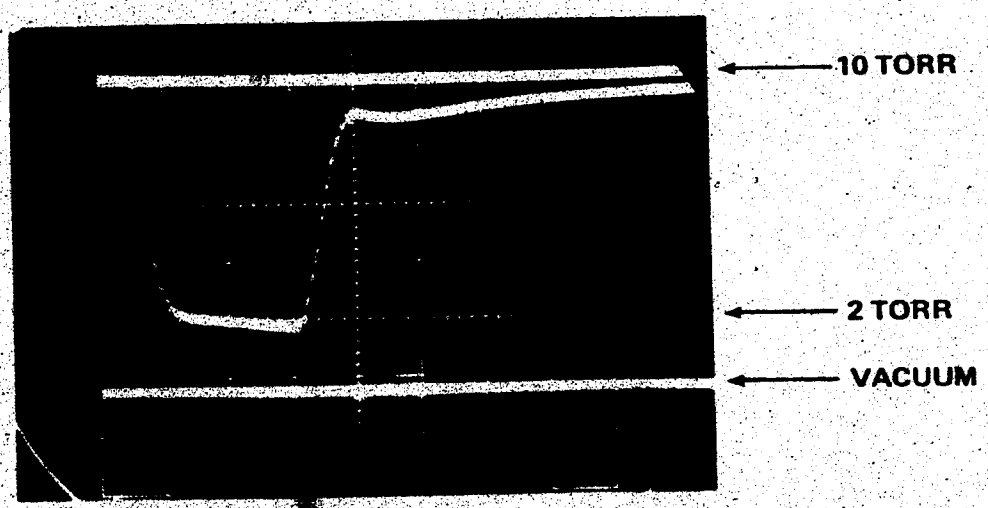
Fig. 10   Pressure Profile across Iris after Valve is
pulsed open

region 1 (Fig. 9), the gas in this region was pumped into the vacuum tank due to the existing pressure gradient when the electromagnetic valve was opened. The valve was pulse activated (Appendix I) and remained open for approximately 0.4 seconds before the rest of the system was triggered. The iris essentially limited the conductance of gas from region 2 to region 1 following valve opening. With a Granville-Philips capacitance manometer, the measured pressure ratio across the iris was at least a factor of five[42], dependent on the iris size (see Fig. 10). With this arrangement, breakdown initiated at the iris propagated (forward) into region 2 along the solenoid axis and underdense plasma was created.

(3) Overall Operation Procedures.

(i) systems and tanks evacuated

(ii) electromagnetic valve closed

(iii) system backfilled with gas at low pressure as desired

(iv) system firing trigger would trigger a one-shot monostable multivibrator (Appendix I) to open the electromagnetic valve; the delayed multivibrator output would trigger the remaining system (see section under "Timing Sequence and Synchronization" in this Chapter).

3.4 The Magnetic Field

(1) Physical Structure (Fig. 11)

The five turn helical solenoid used had a 4 cm diameter bore and was 17 cm long machined from solid brass. The high
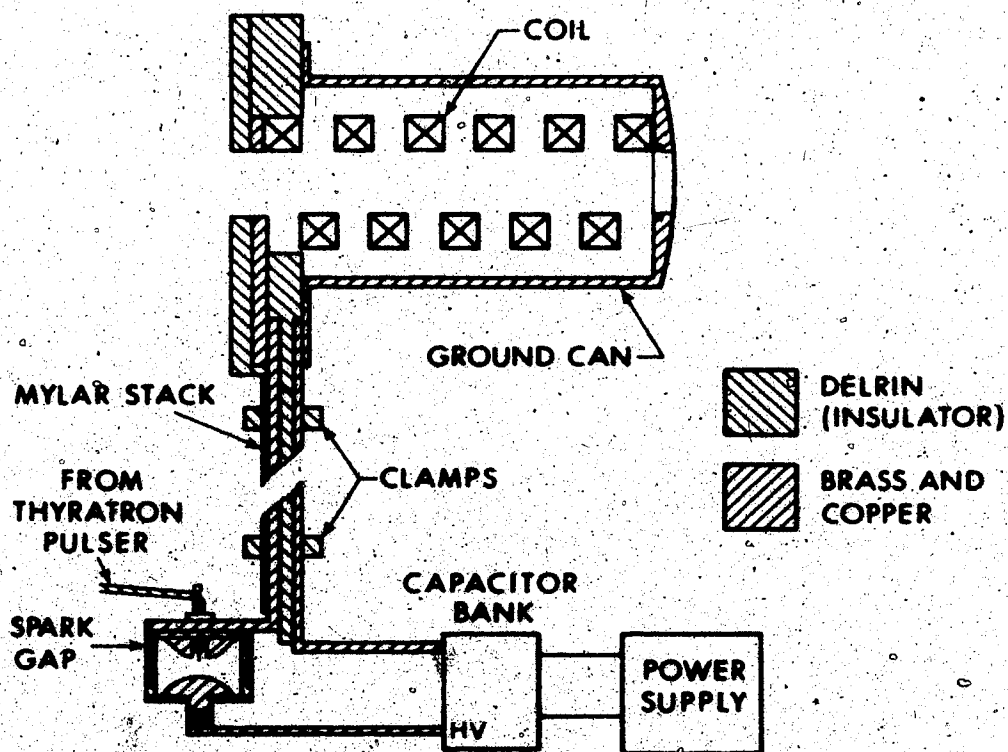
Fig. 11   Cross-section of Coil and Attachment
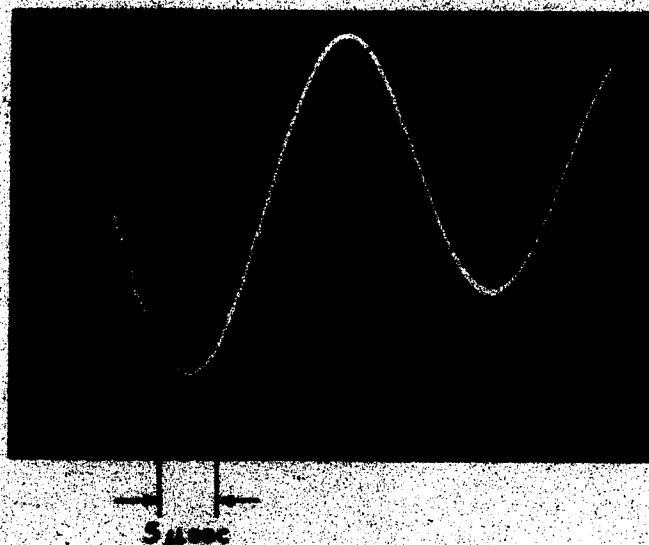
Fig. 12   Induced E.M.F. on Search Coil by 110 K Gauss Field

voltage end of the coil was triggered by a thyratron pul-ser. The ground end of the coil was a coaxial can. Parallel-plate transmission lines were used to connect the capacitor bank. The system was designed to minimize inductance in the configuration apart from the coil itself.

(2) Electrical

Energy stored in the capacitor bank was transformed to magnetic energy in the coil whenever the spark gap was triggered. The breakdown voltage of the spark gap could be as high as 20 KV depending on the separation of the main spark gap electrodes. The maximum energy stored was

$$\tfrac{1}{2}CV^2 = \tfrac{1}{2} \times 87 \times 10^{-6} \times (20 \times 10^3)^2$$

$$= 17.4 \text{ K Joules}$$

(3) B Field Analysis

(i) Model: The overall circuit behaviour was essentially an L-C-R discharge giving a damped sinusoidal current:

$$I = \frac{Ve^{-\beta\omega_0 t}}{\omega_0 L \sqrt{1-\beta^2}} \sin \omega_0 \sqrt{1-\beta^2}\; t$$

where

$$\omega_0 = \frac{1}{\sqrt{LC}}$$

and

$$\beta = \frac{R}{2}\sqrt{\frac{C}{L}}$$

Provided β is small (i.e. R is very small which was the case in this discharge circuitry) $\omega \sqrt{1-\beta^2} \simeq \omega_0$. From the photo in Fig. 12, β could be found from the envelope $e^{-\beta\omega_0 t}$ of the damped current, yielding $\beta \simeq 0.067$ and ω_0 could be found from the period of oscillation $\tau = 28$ μsec, giving $\omega_0 \simeq 2.3\times10^5$ sec^{-1}.

(ii) Measuring Method

The field was measured using a search coil of 1.85 cm diameter having a resistance of 50Ω. The flux cutting the coil induced an e.m.f. given by Faraday's Law, i.e.

$$|E| = \left|\frac{d\Phi}{dt}\right|$$

$$= \frac{d(BA)}{dt}$$

$$= BA\omega_d \cos\omega_d t.$$

Due to 50Ω matching, the amplitude of E measured should include a factor of 2, and assuming $\omega_d \simeq \omega_0$.

$$B = 2|E| \frac{1}{\pi r^2} \frac{1}{\omega}$$

$$= \frac{2|E|}{2.3\times10^5 \times 2.7\times10^{-4}} \text{ Wb/m}^2$$

$$= \frac{20|E|}{61.2} \text{ K Gauss}$$

The results are summarized in Table II.

Theoretical	Experimental
Assuming $\beta \ll 1$ $$L \simeq \frac{1}{\omega_0 C} = \frac{(2.8\times10^{-6})^2}{4\pi^2} \times \frac{1}{87\times10^{-6}}$$ $$= 228 \text{ nH}$$ $$I_{max} = \frac{V_0}{\omega L} e^{-\beta\pi/2}$$ $$= \frac{20\times10^3 \times 28\times10^{-6}}{2\pi\times228\times10^{-9}} \times 0.9$$ $$\simeq 368 \text{ K Amp}$$ $$B_{\text{along axis}} \simeq \frac{\mu_0 N I}{\ell}$$ $$= 4\pi\times10^{-7}\times\frac{5}{0.17}\times368 \text{ Wb/m}^2$$ $$= 136 \text{ K Gauss}$$	$$|E| = 320 \text{ V measured}$$ $$B = \frac{20|E|}{61.2} \text{ K Gauss}$$ $$= 111 \text{ K Gauss}$$

Table II Magnetic Field Calculations and Measurements

3.5 Laser Power Attenuator

An attenuator cell was placed in the optical path (Fig. 8) to vary incident power to the plasma cell. This type of cell was used by Offenberger et al[43] as a high power CO_2 laser energy detector. Basically the cell had NaCl windows fitted on each end containing a few Torr of propylene (C_3H_6) with helium buffer gas at a total pressure of 700 Torr.[44] Laser beam transmission decreases exponentially with propylene partial pressure and thus the laser

power could be conveniently adjusted. In practice, the actual transmission was measured using infrared detectors and calorimeters as conditions were varied. Propylene partial pressures of 0-20 Torr were used in the present experiment.

3.6 Optics and Red-Shift Measurement

The optics along the backscattered collection path included monochromator, Fabry-Perot interferometer, filters and detector. As mentioned, alignment of optics in this path was checked frequently to assure stability of the system in view of floor vibration due to mechanical pumps and temperature dependent behaviour of the Fabry-Perot interferometer. With the alignment lasers, the overall optical system gave very reproducible results.

(1) Monochromator

Backscattered light collected from the beam splitter was focussed with a 45.7 cm focal length mirror onto the entrance slit of a half meter monochromator for pre-dispersion. The output was recollimated with a NaCl lens for high resolution spectral analysis in a Fabry-Perot interferometer and subsequently detected with a variety of doped Ge detectors.

Monochromator characteristics are summarized in Table III.

Item	
Grating	Echelle
Grating Area	85 mm×76 mm
Number of ruled lines per mm	75
Resolving Power in first order	76×75 = 5700
Grating blazed for	8 μ
Dispersion of monochromator at exit	270 Å/mm
Focal length	45.7 cm

Table III   Monochromator Characteristics

(2) Fabry-Perot Interferometer

While the monochromator had a dispersion of 270 Å/mm, the high finesse piezoelectric-scanning interferometer provided resolution of a few angstroms, thus enabling highly resolved scattered spectra to be measured.

The interferometer is a two mirror resonant cavity with one mirror fixed and the other one piezoelectrically moved by an adjustable high voltage which could be scanned manually or ramped repetitively. The movable mirror was mounted on a dove-tailed rail. Mirror parallelism could be attained by horizontal and vertical adjustment of two micrometers.

Interferometer characteristics were markedly influenced by the ever-changing ambient temperature producing a drift in wavelength. To minimize this change, the interferometer was placed in a well-insulated styrofoam box. Alignment was checked frequently and adjusted as necessary
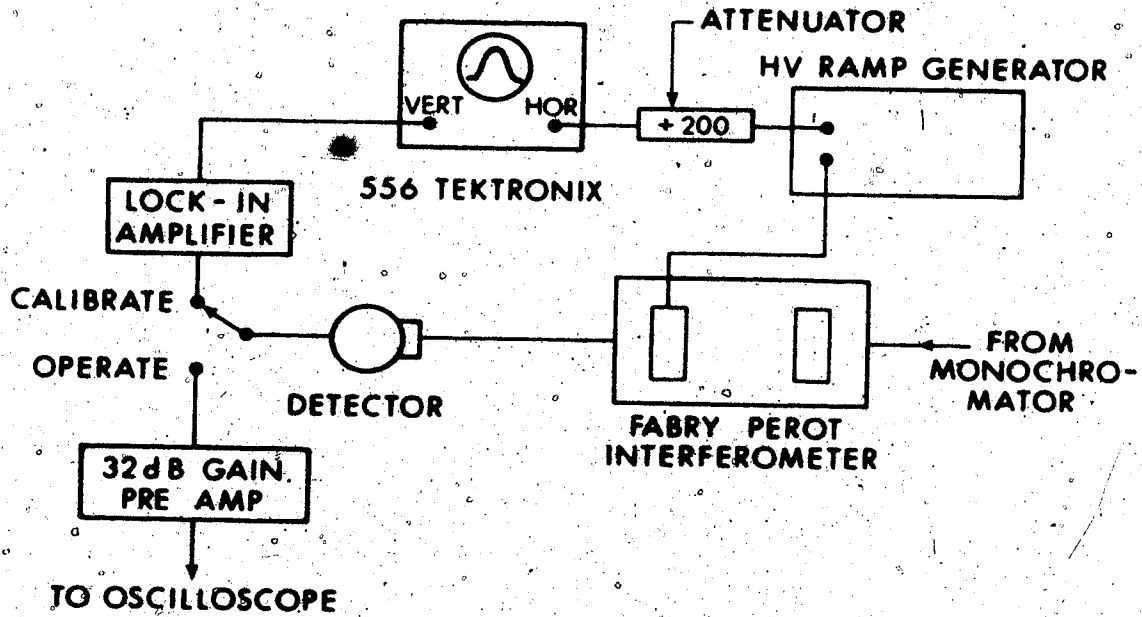
Fig. 13   Fabry-Perot Interferometer Calibration and
Operation Schematic
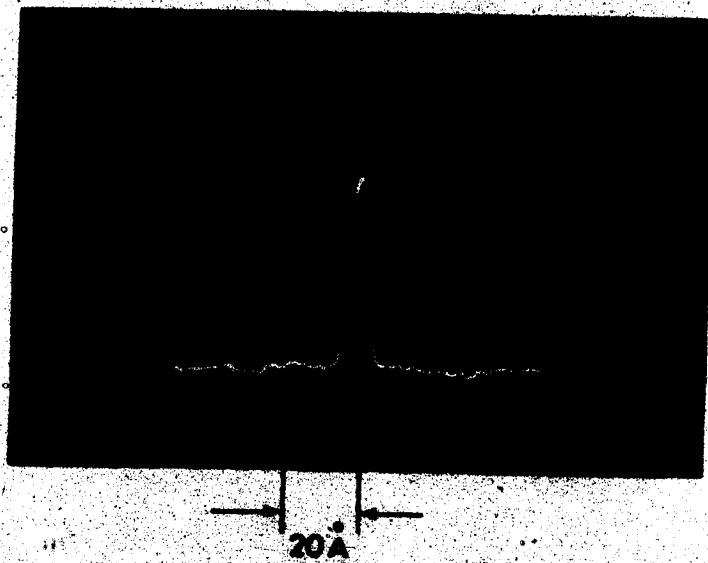
Fig. 14   Spectral Resolution of F.P.I.

(see step "d" in alignment procedure).

(i) Alignment Procedure

The alignment procedure for the Fabry-Perot interferometer is illustrated in Fig. 13.

a) With switch shown in "calibrate" position, the movable germanium mirror was brought to a distance of 1 mm from the first mirror.

b) Attenuated chopped-CW CO_2 laser radiation (laser linewidth ~ 0.2 Å) was let through. Micrometers were adjusted to attain the highest resolution (Fig. 14 illustrated a resolution of 4.5 Å).

c) Ramp output; horizontal gain and horizontal position of oscilloscope (Tektronix 556) were adjusted such that a range of wavelength shift of -40 Å to +140 Å would be covered with the reference wavelength to 0 Å.

d) Frequently, the alignment was checked. If the peak transmitted laser signal reference drifted from the no-shift-position (0 Å), the magnitude of drift was recorded to correct measured shift and laser signal was brought back to no-shift-position by adjustment of the horizontal position knob.

(ii) Analysis of the Piezoelectric scanning F.P.I.

Knowing the separation of mirrors, d = 1 mm and the scan range of ramp $\Delta V = 1,600V$, we can calculate the wavelength variation with applied voltage. Now the reinforcement of the transmitted ray is given by[45]

$$2d\cos\theta = m\lambda \text{ where } m = \text{order of interference}$$

or for normal incidence

$$2d = m\lambda \qquad\qquad\qquad (i)$$

The free spectral range, i.e. the wavelength interval in a given order when the fringe of the same wavelength in the next higher order is reached, is[45]

$$\Delta\lambda_s \simeq \frac{\lambda^2}{2d} = \frac{(10.59\times10^{-6})^2}{.2\times10^{-3}} = 560 \overset{\circ}{A}$$

from (i)

$$2(d+\Delta d) = m(\lambda+\Delta\lambda) \qquad \frac{\Delta\lambda}{\lambda} = \frac{\Delta d}{d} \qquad\qquad (ii)$$

For this particular piezoelectric stack, the linear exten-sion is 4.4 μ in 1,600 V, or the sensitivity of the ramp it-self is

$$\frac{\Delta d}{\Delta V} = \frac{4.4 \ \mu}{1600 \ V} = 27.5 \ \overset{\circ}{A}/V \ .$$

Therefore the wavelength sensitivity of the ramp-interfero-meter is

$$\frac{\Delta\lambda_{scan}}{\Delta V} = \frac{\Delta\lambda_{scan}}{\Delta d} \cdot \frac{\Delta d}{\Delta V}$$

$$= \frac{\lambda}{d} \cdot \frac{\Delta d}{\Delta V}$$

$$= \frac{10.59\times10^{-6}}{1\times10^{-3}} (27.5) = 0.29 \ \overset{\circ}{A}/V \ .$$

Consequently, one volt increase in the linear ramp corres-ponds to 0.29 $\overset{\circ}{A}$ change in wavelength.

(3) Red-shift Measurements

After aligning the horizontal time base of the oscillo-
scope to cover a spectrum of -40 Å to +140 Å with no-shift-
position at 0 Å, the lower limit of the ramp was adjusted to
select a particular Δλ shift display before the laser was
fired. With a digital voltmeter to monitor the attenuated
ramp to the horizontal input of the oscilloscope and the
beam spot moved to varying wavelength shift positions, the
spectrum could be scanned very accurately. Of course, the
correction on Δλ due to temperature drift of F.P.I. had to
be checked regularly. Laser backscattered signals were
observed and recorded several times for each Δλ value.

(4) Filtering and Attenuation

Various narrow band filters were used to provide wave-
length discrimination at 10.6 μ and also other wavelengths
in a search for Raman scattering. In addition, series com-
binations could be used to determine relative amplitudes.

It was also necessary to employ mylar attenuators to
reduce the observed scattered signal to levels where the
detectors would respond linearly. These were calibrated
using CW CO_2 laser radiation.

3.7 Detectors

Several cooled infrared detectors were used in this
experiment. The following table gives a comparison of all
three which had been used. (Data shown with a 50Ω termina-
tion).

Photon-sensing chip	Temperature cooled to	Sensitivity at 10.6μ	Response Time
Ge : Hg	Liquid helium	500 V/watt	~ 100 nsec
Ge : Cu	Liquid helium	30 V/watt	~ 2 nsec
Ge : Au	Liquid nitrogen	~ 0.2 V/watt	~ 1 nsec

Table IV   Characteristics of Different Detectors

The gold-doped detector was used chiefly for pulse monitoring because of its high speed, low sensitivity characteristics. The higher sensitivity of the mercury-doped detector was used for spectral runs. Finally, the copper-doped detector was used to provide both adequate speed and sensitivity for many measurements.

3.8 High Speed Photography

Laser induced gas breakdown hydrodynamics were studied using a TRW image converter camera with high speed streak plug-in units. The plug-in unit used was a Model 7B which has streak writing times of 50, 100, 200 nsec in a five centimeter streak. Again, camera triggering was synchronized to follow the evolution of plasma. Longitudinal streak photos were taken to ensure iris function and to determine plasma column length.

3.9 Firing Sequence And Synchronization

The electromagnetic valve opening with subsequent gas pumping was activated prior to all other events. Following this, synchronized firing of the pulse CO_2 laser, streak
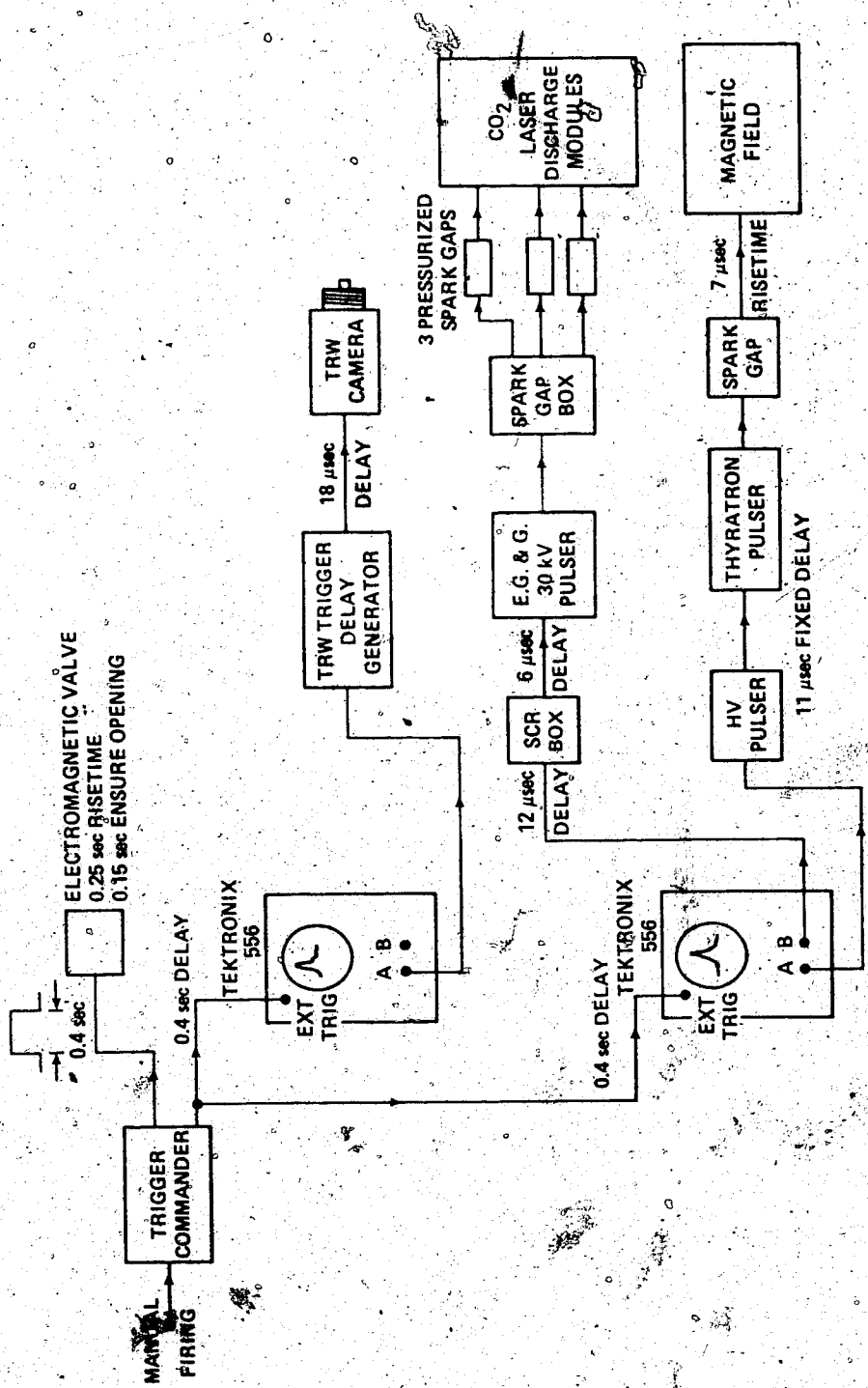
Fig. 15   Firing Sequence and Synchronization

camera and the capacitor bank discharge through the magnetic

field coil was initiated. The trigger commander box

(Appendix I), once triggered, opened the electromagnetic

valve long enough (~ 0.4 sec) for gas to be evacuated into

the vacuum tank. After this delay, a 5 V trigger pulse from

the box was used to trigger two Tektronix 556 oscilloscopes.

The undelayed and delayed gates of the oscilloscopes were

utilized to trigger laser; magnetic field and streak camera

circuits. The overall firing sequence and synchronization

are sketched in Fig. 15. Synchronization of laser, streak

camera and peak magnetic field were monitored on every

shot and showed excellent reproducibility.

200 nsec

100 nsec

Vacuum

Plasma

(a)

(b)

(c)

(d)
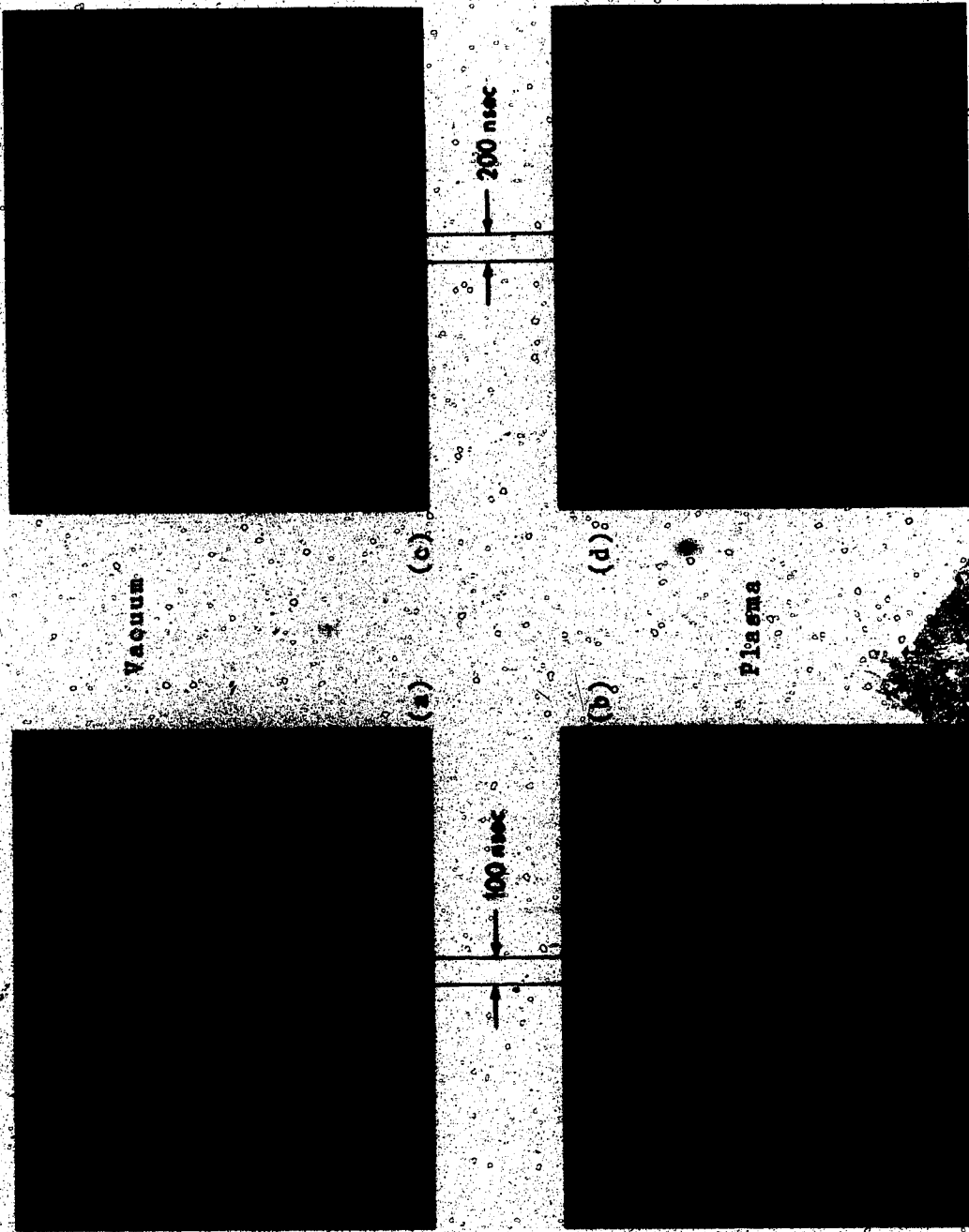
Fig. 16. Laser Pulse Shapes
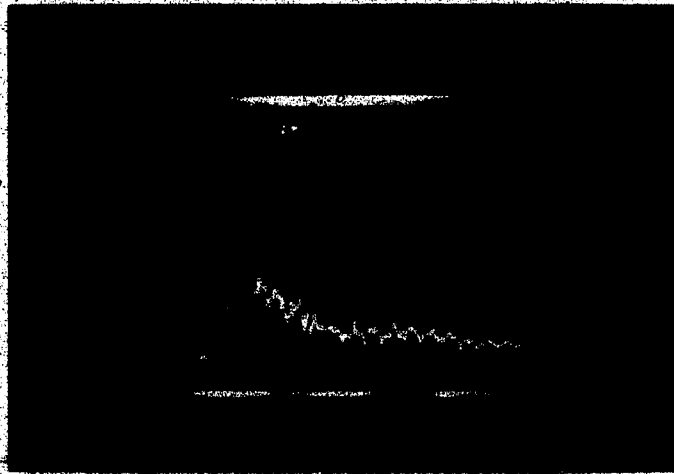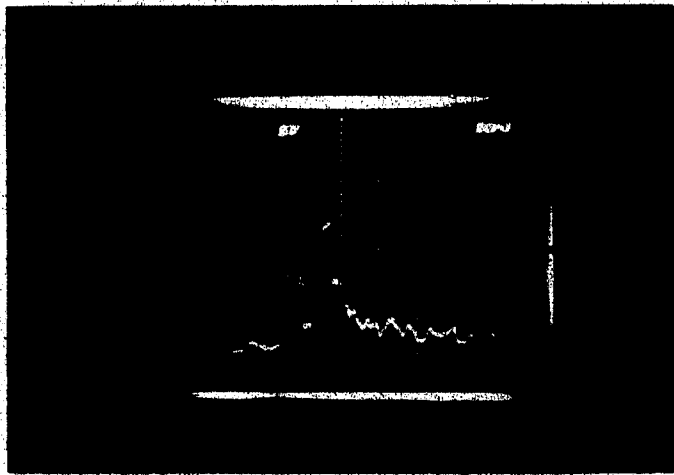
Fig. 17   Sample Oscillogram of Backscattered Signal

CHAPTER IV

RESULTS

Data for the temporal and spectral characteristics of the backscattered signal will be presented and analysed in the following sections. Comparison with both analytic and numerical integration of the growth rate as theoretically derived by Tsytovich will be made. Good agreement is found between theory and experiment.

4.1 Pulse-Shape

(1) Laser Pulse Shape

Laser pulse shapes as obtained with the copper doped germanium detector cooled to 4°K are as shown in Fig. 16. Time bases for illustrating temporal characteristics are 100 nsec and 200 nsec. The initial pulse has a FWHM of 40 nsec with peak power of $\simeq$ 1 Gigawatt and the lower power tail lasts for approximately 1 μsec.

Fig. 16(b) and (d) were taken with gas backfill and consequently laser induced breakdown creating a plasma column. From these photos, laser transmission decreases due to absorption of energy by the plasma created gas breakdown. Breakdown without magnetic field occurs at roughly two-thirds of the peak power. Laser plasma interaction begins at this time and stimulated backscattering builds up as a temporal folding of laser intensity and plasma column length.

(2) Backscattered Signal Pulse Shape

Backscattered light was collected by the optical system outlined in last Chapter. To optimize sensitivity and speed of detection of the backscattered light, different detectors of suitable sensitivity and response were used. Illustrative pulse shapes obtained with the copper-doped detector and displayed on a Tektronix 7904 oscilloscope are as shown in Fig. 17.

The major temporal characteristics of these backscattered signals are as follows: (i) They are prompt signals with very small delay measured between plasma creation and back-scattered signal peak and average over a large number of shots are around 15 to 25 nanoseconds. This represents the time necessary for an adequate plasma length to be formed to generate a sufficient number of nonlinear wave e-foldings. (ii) The three photos shown here are only a few out of many hundred shots. They reveal the extreme cases of how the backscattered signal shape can vary from shot to shot. The randomness of these pulse shapes is governed by laser output, gas-plasma evolution and nonlinear interaction. Hence the risetime and amplitude is bound to change depending on the slight difference in time history of these factors from shot to shot. Moreover, the appearance and disappearance of back-scatter is attributed to build-up and decay of ion waves. However, the more usual case was that of single backscattered pulses and the data used for spectral analysis was taken from these shots. (iii) Though the pulse shape seldom
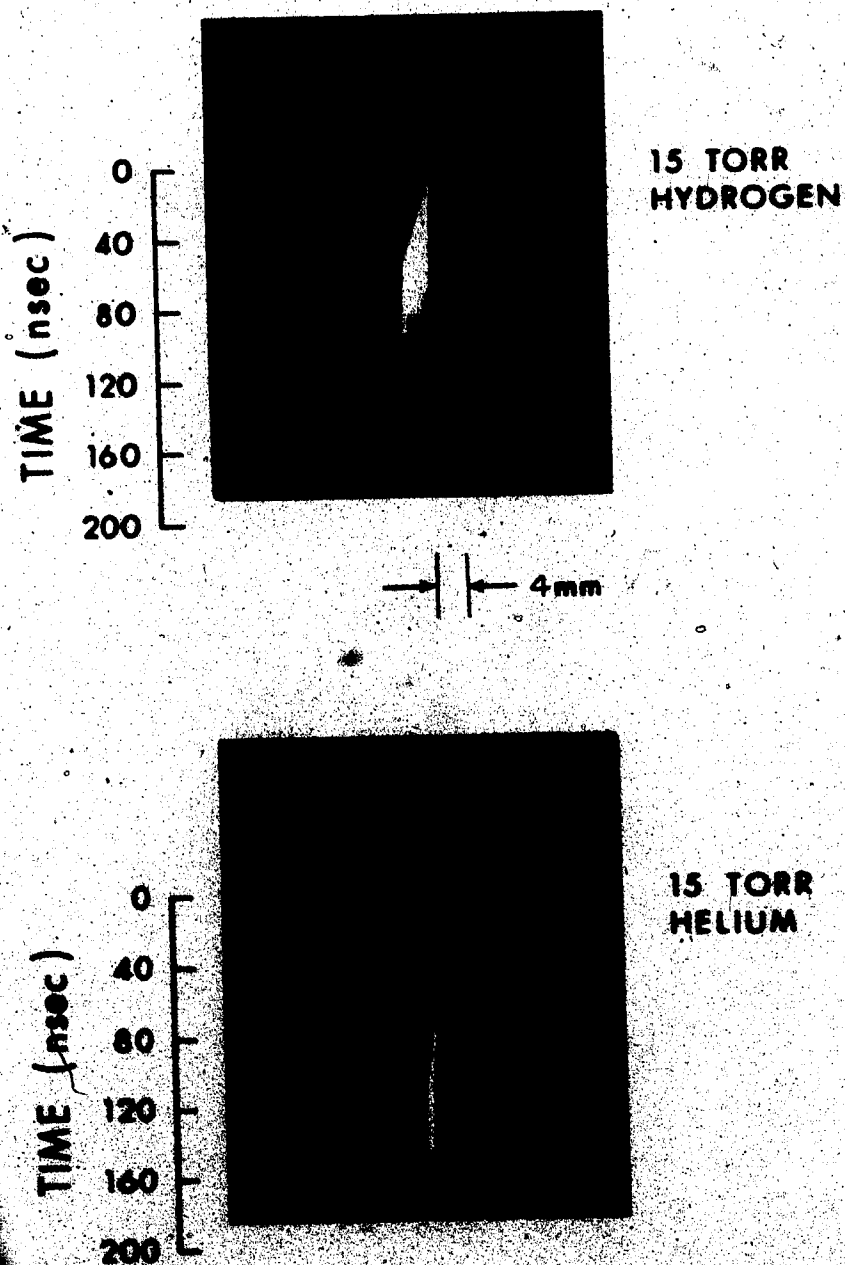
Fig. 18   Streak Photos of Laser Induced Breakdown in
15 Torr Hydrogen and Helium Plasma Column

reproduce identically, they show good signal to noise ratio which completely dominates stray light. To achieve this situation it was necessary to enclose the optical path with black cloth to eliminate stray light. Only at the lowest levels of backscattered light in spectral runs was it necessary to subtract out any stray light background. In short, the stimulated backscattering power considerably exceeded the noise level; a ratio of $\approx 400/1$ was found in practice.

To prevent saturation of the detector which may obscure the time signal, mylar sheets of calibrated attenuation were used at the entrance to the monochromator. The combined rise time of the Ge:Cu detector, preamplifier and oscilloscope displays are approximately 2.3 nsec for the 7904 oscilloscope and approximately 7 nsec for the 556 Tektronix.

4.2 Axial Streak Photos

The streak photos shown in Fig. 18 were taken using a 200 nsec streak plug-in unit with a TRW streak camera. Fig. 18(a) illustrates the time and space profile of the 15 Torr hydrogen plasma column formation along the optical axis. Fig. 18(b) shows the same information for the 15 Torr helium plasma column formation.

With reference to these photos, it can be seen that in the first two hundred nanoseconds, due to the presence of the 4.5 mm diameter aluminum iris placed at the focus, there exists only one breakdown front travelling in the same direction as the incoming laser (from right to left on paper). This
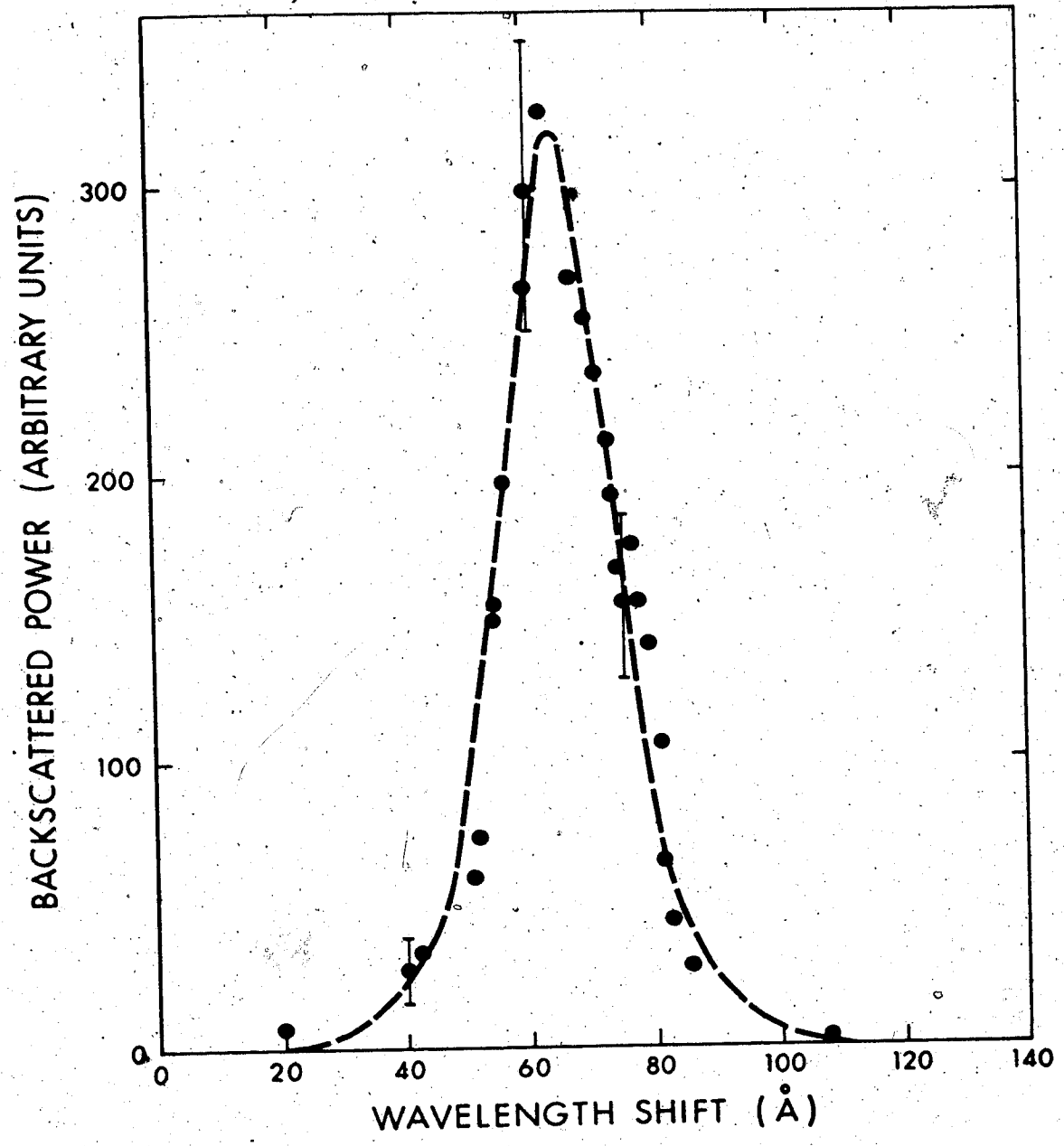
Fig. 19   Spectrum of Backscattered Power for Non-
magnetically Confined Hydrogen Plasma
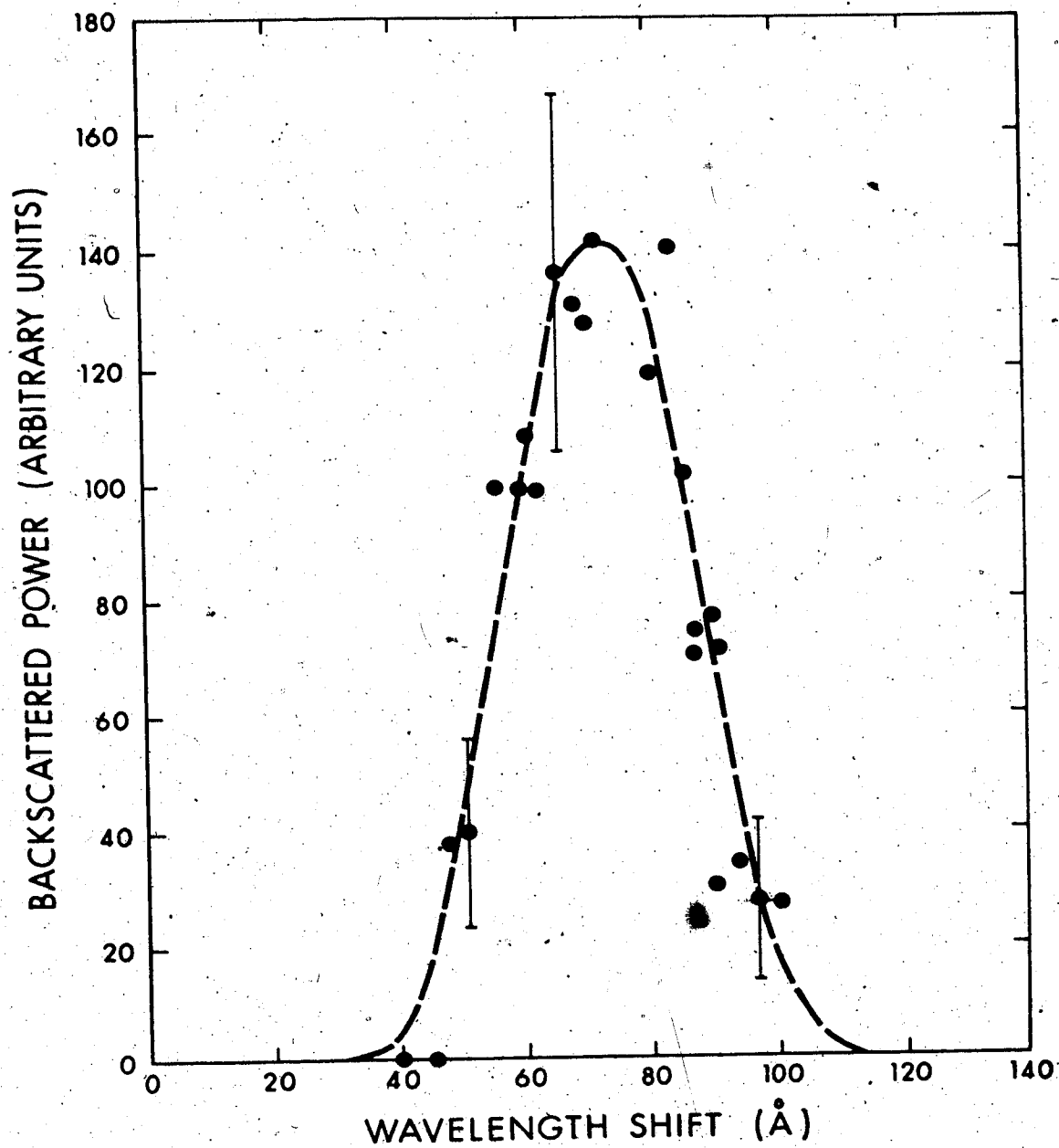
Fig. 20   Spectrum of Backscattered Power for Hydrogen
Plasma Confined by an Axial 110 K Gauss Mag-
netic Field

shows nicely the purpose of the iris in fast evacuation of gas in the front end before laser firing so that no absorption of laser power occurs ahead of the iris.

Notice that the wavefront of the breakdown travels at a constant speed during this time and is 2×10^7 cm/sec for the hydrogen case and 9×10^6 cm/sec for the helium plasma. For 18 Torr hydrogen the breakdown speed is 2.2×10^7 cm/sec. With this information and taking an average time of 20 nsec to the peak of the backscattered signal following gas break-down, the plasma length can be determined as 4.4 mm long for hydrogen at 18 Torr.

4.3 Red-shift

Spectrally resolved backscattered power averaged over many shots and further averaged over a 10Å spectral window (the resolution of the Fabry-Perot interferometer was 4.5Å) can be used to calculate the ion wave characteristics. Fig. 19 shows the shift of backscattered signal away from the laser line (which is at 0Å) for no magnetic field and Fig. 20 shows the shift for a 100 KGauss axial magnetic field. Note that only positive wavelength shifts were observed. Scans to negative wavelengths with a 100 increased sensitivity showed no backscattered radiation.

Analysis

Now the dispersion relation for ion acoustic waves is given by equation (16) in Chapter II as

$$\omega_i \simeq k_i c_s [1 + \frac{3}{2} \frac{v_i^2}{v_\phi^2}] \qquad (16)$$

where ω_i=ion acoustic frequency, experimentally measured as the shift, k_i=ion wave number=$2k_0$ from equation (2) for back-scatter, $v_i = \sqrt{\chi T_i / m_i}$, $v_\phi = \omega_i / k_i$=phase velocity of the ion wave, $c_s = \sqrt{\frac{\chi T_e}{m_i}}$=ion sound speed. To lowest order $\omega_i = k_i c_s$ which gives an estimate for T_e. Then using ratios for T_e/T_i taken from hydrodynamic calculations[46], a better estimate for T_e can be obtained from equation (16) above.

(1) Zero Magnetic Field Case

The peak of the red-shift for hydrogen occurs at $\Delta\lambda$=65Å±5Å which corresponds to ω_i=1.09×10^{11} sec^{-1}. Since k_i=11855 cm^{-1}, the phase velocity v_ϕ=9×10^6 cm/sec, from which the procedure outlined above gives $T_e \simeq 45$eV and $T_i \simeq 11$eV. This assumes a temperature ratio of 4.

Incidentally, if one takes these values for v_ϕ and T_i, the corresponding x value of Fig. 22 is x=1.95 which is consistent with the spectral shift being a maximum for x≈2 for a temperature ratio T_e/T_i=4.

(2) Non-Zero Magnetic Field Case

The peak of the red shift for hydrogen in this case occurs at $\Delta\lambda$=72Å±5Å. Following the same procedure, but now taking a temperature ratio of 8 to be consistent with hydrodynamic results the corresponding values are v_ϕ=10^7 cm/sec,

$T_e \simeq 74 eV$ and $T_i \simeq 9 eV$.

With reference to Fig. 22, the experimental value $x=2.4$ for $T_e/T_i=8$ agrees well with curve "g" for which a ratio $T_e/T_i=7.6$ corresponds to a peak at $x=2.4$, thus again showing consistency between experiment and theory.

These results are summarized in Table V below:

B	$\Delta\lambda$	T_e/T_i	T_e	T_i
0	65$\overset{o}{A}$	4	~45eV	~11eV
110KG	72$\overset{o}{A}$	8	~74eV	~9eV

Table V. Summarized Redshift of Hydrogen

The one rather surprising feature of the spectrum for the magnetized plasma case is the much broader width and lower amplitude. This is unexpected since for higher T_e/T_i ratio less Landau damping should occur with a consequently narrower width. No explanation can be given at this time for the clearly wider spectrum observed but possibilities include: (i) reduced ion wave amplitude by virtue of higher thermal energy, (ii) increased turbulence and (iii) nonlinear damping.

(3) Case with Helium Plasma (B=0)

The purpose of using helium in lieu of hydrogen is to confirm the ion-acoustic frequency dependence on mass, i.e. $\omega_i \propto \Delta\lambda \propto (m_i)^{-\frac{1}{2}}$. The result is not plotted here but shows a similar spectral profile to hydrogen except the wavelength

shift $\Delta\lambda$ found for this case is $30\text{A}\pm5\text{A}$. Taking into account
the slightly different T_e for helium, this shift shows the
expected reduction, i.e. $\sqrt{m_{H_e}/m_H} = 2$. This confirms the ion
acoustic mode as responsible for the stimulated backscatter.

4.4 Reflectivity of Plasma

As mentioned, the backscattered power was determined
from detector signal amplitudes. The measured signals are a
function of beam attenuation and risetime of the detector
systems. The optical path, exclusive of Fabry-Perot, namely
two beam-splitters, mirrors and monochromator was found in
calibration to have a combined transmission of 1%. Two
different sensitive detectors were used in the measurements
and the power reflectivity factors are tabulated below.

Detector / List	Ge:Hg	Ge:Cu
Response	Slow 100 nsec	Fast 2 nsec
Response Compensation	20	1
Sensitivity	500 V/watt	30V/watt
Attenuation Added	$(20)^5$	$(20)^5$
Amplification by Pre-amplifier	32	32
Path Transmission	1%	1%
Signal detected	3 volts	3 volts
Power Reflected	$\dfrac{3\times(20)^5\times20}{500\times32\times\frac{1}{100}} = 1.2\text{MW}$	$\dfrac{3\times(20)^5\times1}{30\times32\times\frac{1}{100}} = 1\text{MW}$

Table VI   Reflectivity of Plasma Measurement

Since the maximum of the backscattering occurs somewhat after the peak of the initial laser pulse, we can assume the average incident power to be ≃500MW. Therefore the percentage power reflectivity of the plasma is approximately $\frac{1MW}{500MW}\times100\%\approx0.2\%$ i.e. only 0.2% of the input laser power was observed in back-scatter. As we shall see, no apparent saturation of back-scatter signal with incident intensities up to 10^{11} watts/cm^2 was observed.

4.5 Experimental Backscatter Growth Rate γ

With 18 Torr of hydrogen backfill and incident laser power controlled by a propylene-helium absorption cell, the measured backscatter power is plotted as function of incident power in Fig. 21. Data points, along with error bars are average signals obtained from many shots. Incident power was determined by measuring cell transmission after propylene pressure changes.

From Fig. 21, obviously the backscattered power increases exponentially as incident laser power increases. The slope of the line in Fig. 21 determines the exponential growth rate of the backscattered light as a function of incident laser intensity. From equation (14a) with e-foldings defined as $\gamma\equiv\gamma_0 I$, it leads to

$$N_2 = e^{\gamma_0 I_1 t} = e^{\gamma_0 \alpha I_0 t}$$

$$N_1 = e^{\gamma_0 I_2 t} = e^{\gamma_0 \beta I_0 t}$$
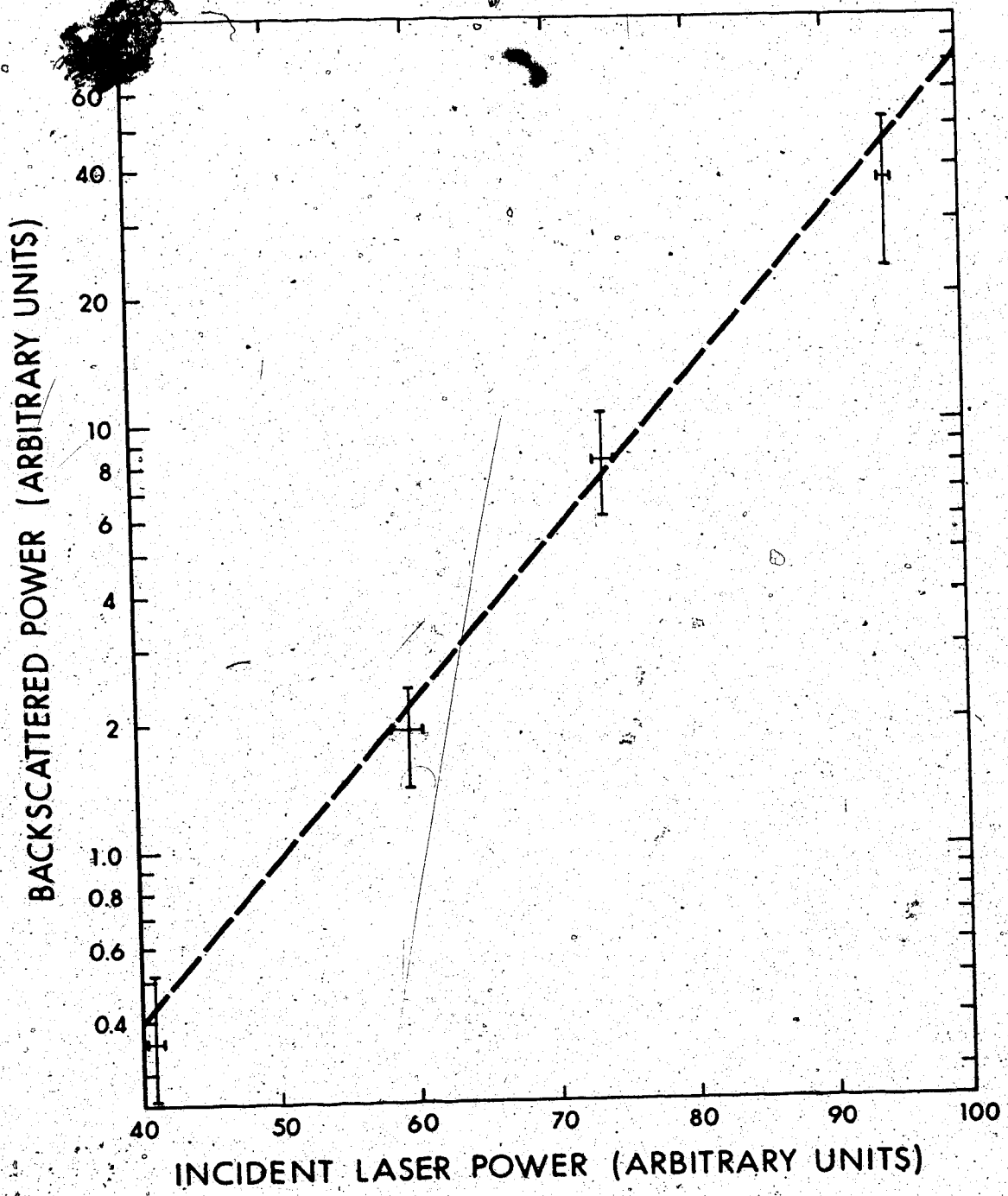
Fig. 21   Backscattered Power Versus Incident Laser Power

where I_0 is the full laser intensity and α, β are transmission coefficients of the absorption cell, N_2 and N_1 can be read off from the ordinates of Fig. 21. Hence

$$\frac{N_2}{N_1} = e^{\gamma_0 I_0 (\alpha - \beta) t}$$

substituting two data points in the above expression,

$$\frac{7.5}{0.4} = e^{\gamma_0 I_0 (1 - 0.4) t}$$

with I_0 known to be 10^{11} watts/cm^2, the e-foldings become

$$\gamma_0 I_0 t = 8.7$$

$$\gamma_0 I_0 \frac{\ell}{c} = 8.7$$

$$\gamma \equiv \gamma_0 I_0 = \frac{8.7 \times 3 \times 10^{10}}{0.44}$$

experimental $\gamma = 5.93 \times 10^{11}$ sec^{-1}

Equivalently, the scale length for growth of scattering is $\frac{0.44 \text{ cm}}{8.7} = 0.05$ cm which is approximately equal to 50 laser wavelengths.

If on the other hand, the experimental growth rate were interpreted directly in terms of finite length, coherent wave theory, then since the backscattered wave amplitude grows exponentially as $\gamma_0^2 \ell / \gamma_i c$, the power would vary as

$$P_B = P_N \exp \frac{2\gamma_0^2 \ell}{\gamma_i c}$$

where P_N is noise level.

Experiment gives 8.7 e-foldings as $\gamma_i \equiv 3.5 \times 10^{10}$ sec^{-1} whereby

$$\gamma_0 = [\frac{(8.7)(3.5\times 10^{10})(3\times 10^{10})}{2(0.44)}]^{\frac{1}{2}}$$

$$\simeq 10^{11} \text{ sec}^{-1} .$$

This is a factor of 6 lower than the value interpreted from random phase theory which is somewhat surprising, inasmuch as a larger value might intuitively be expected.

We now turn to theoretical calculations of these values.

4.6 Computer Solution to Tsytovich's Prediction of γ

We have determined an experimental value for the growth rate of stimulated Brillouin scattering $\gamma = 5.93 \times 10^{11}$ sec^{-1} which can be compared with the theoretical value. This requires integration of Equation (14) after appropriate substituting for the laser spectral intensity in $N_{k'}$.

Now electron and ion permittivities are given by

$$\varepsilon_{e,i} = 1 - \frac{\omega_{pe,pi}^2}{k_i^2} \int \frac{k_i \frac{\partial f_{e,i}}{\partial u}}{\omega - k_i u} du$$

where

$$k_i = |\underline{k} - \underline{k}_0| .$$

In the case where $u_e \gg \frac{\omega}{k_i}$, the permittivity for electrons reduces to

$$\varepsilon_e = 1 - \frac{\omega_{pe}^2}{k_i^2} \left(-\frac{m_e}{\chi T_e}\right)$$

$$= 1 + \frac{4\pi n_0 e^2}{m_e} \frac{m_e}{\chi T_e} \frac{1}{k_i^2}$$

$$= 1 + \frac{1}{k_i^2 \lambda_D^2}$$

$$= 1 + \alpha^2$$

where $\alpha \equiv \dfrac{1}{k_i^2 \lambda_D^2}$ with λ_D the Debye length and from Salpeter[31],

ε_i may be expressed as

$$\varepsilon_i = 1 + \alpha^2 \frac{T_e}{T_i} F(x)$$

with $F(x) = 1 - 2xe^{-x^2} \int_0^x e^{t^2} dt + i\sqrt{\pi}\, xe^{-x^2}$

since $\varepsilon = \varepsilon_e + \varepsilon_i - 1$

$$\frac{|\varepsilon_e - 1|^2}{|\varepsilon_e + \varepsilon_i - 1|^2} = \frac{[\alpha^2]^2}{\left|\alpha^2 + 1 + \alpha^2 \dfrac{T_e}{T_i} F(x)\right|^2}$$

$$= \frac{\alpha^4}{(1+\alpha^2)^2 \left|1 + \dfrac{\alpha^2}{1+\alpha^2} \dfrac{T_e}{T_i} F(x)\right|^2}$$

$$= \left(\frac{\alpha^2}{1+\alpha^2}\right)^2 \frac{1}{|1 + \beta^2 F(x)|^2}$$

where $\beta^2 = \frac{\alpha^2}{1+\alpha^2} \frac{T_e}{T_i} \simeq \frac{T_e}{T_i}$ if $\alpha^2 >> 1$.

This is satisfied for ion-acoustic waves of interest in the present experiment, hence.

$$\frac{|\epsilon_e - 1|^2}{|\epsilon_e + \epsilon_i - 1|^2} \simeq \frac{1}{|1 + \beta^2 F(x)|^2} \tag{17}$$

using Salpeter's notation defining

$$\Gamma_\beta(x) \equiv \frac{e^{-x^2}}{|1 + \beta^2 F(x)|^2} \tag{18}$$

also from (14), γ_k can be re-arranged as

$$\gamma_k = \frac{\hbar}{(2\pi)^3 m_i} \int d\underline{k}' W_p N_{k'} \int (\underline{k} - \underline{k}') \cdot \frac{\partial f}{\partial \underline{v}} \delta[\Delta\omega - \Delta\underline{k} \cdot \underline{v}] d\underline{v}$$

where W_p, the probability of scattering a transverse wave into another transverse wave by plasma ions is given by (13):

$$W_p = \frac{(2\pi)^3 e^4}{m_e^2 2\omega\omega'} [1 + \frac{(\underline{k} \cdot \underline{k}')}{k^2 k'^2}] |\frac{\epsilon_e - 1}{\epsilon}|^2.$$

The dot product in γ_k show only velocity components along $(\underline{k} - \underline{k}')$ are involved; therefore if a Maxwellian distribution of ions is assumed as

$$f = n_0 \sqrt{\frac{m_i}{2\pi\chi T_i}} e^{-\frac{m_i}{2\chi T_i} v^2}$$

$$-(\frac{m_i}{\chi T_i})\underline{v}f$$

where $\underline{v}$ is along $|\underline{k}-\underline{k}'|$

$$\int_{-\infty}^{\infty} (\underline{k}-\underline{k}') \cdot \frac{\partial f}{\partial \underline{v}} \, d\underline{v} \, \delta[\Delta\omega - \Delta\underline{k} \cdot \underline{v}] = \int_{-\infty}^{\infty} - \frac{m_i}{\chi T_i} \, uf\delta[u - \frac{\Delta\omega}{|\Delta\underline{k}|}]du \quad .$$

This integration yields $= -\frac{m_i}{\chi T_i} \frac{\Delta\omega}{|\Delta\underline{k}|} \sqrt{\frac{m_i}{2\pi\chi T_i}} \; e^{-\frac{m_i}{2\chi T_i}(\frac{\Delta\omega}{|\Delta\underline{k}|})^2}$

so $\gamma_k = \frac{\hbar}{(2\pi)^3 m_i}(-\frac{m_i}{\chi T_i})\sqrt{\frac{m_i}{2\pi\chi T_i}} \; n_0 \int \frac{\Delta\omega}{|\Delta\underline{k}|} W_p \; e^{-\frac{m_i}{2\chi T_i}(\frac{\Delta\omega}{|\Delta\underline{k}|})^2} \, d\underline{k}' \quad .$

Putting W_p in γ_k and noting that $\omega'=k'c \simeq k_0 c$, $\omega = kc \simeq k_0 c$ and

$1 + \frac{(\underline{k}\cdot\underline{k}')^2}{k^2 k'^2} \simeq 2$ for backscatter, then

$$\gamma_k = \frac{-\hbar}{\chi T_i} \sqrt{\frac{m_i}{2\pi\chi T_i}} \frac{n_0 e^4}{m_e^2} \int_{-\infty}^{\infty} \frac{N_{k'}}{k_0^2 c^2} \frac{\Delta\omega}{|\Delta\underline{k}|} \frac{e^{-\frac{m_i}{2\chi T_i}(\frac{\Delta\omega}{|\Delta\underline{k}|})^2}}{|1+\beta^2 F(x)|^2} \, d\underline{k}'$$

$$= -\frac{e^4}{m_e^2 c^2} \frac{\hbar n_0}{\chi T_i} \sqrt{\frac{m_i}{2\pi\chi T_i}} \int_{-\infty}^{\infty} \frac{\Delta\omega}{|\Delta\underline{k}|} \frac{N_{k'}}{k_0^2} \frac{e^{-\frac{m_i}{2\chi T_i}(\frac{\Delta\omega}{|\Delta\underline{k}|})^2}}{|1+\beta^2 F(x)|^2} \, d\underline{k}' \quad .$$

$$\tag{19}$$

Since $F(x)=1-2xe^{-x^2}\int_0^x e^{t^2} dt + i\sqrt{\pi}e^{-x^2}x$ is tabulated by Fried and

Conte[47], γ_k can be solved depending on the laser spectrum

$N_{k'}$. $N_{k'}$ is the spectral density on the incoming quanta

and solutions are obtained for two different spectral profiles

in the following evaluation

(1) Gaussian Laser Spectrum

(i) γ_k evaluation via numerical integration

Assuming a Gaussian spectrum of width ℓ' (experimentally known), then

$$N_k' = \frac{(2\pi)^3 I \ell' e^{-\ell'^2 (k'-k_0)^2}}{\hbar \omega c \sqrt{\pi} k'^2 \Delta\Omega}$$

substituting $a^2 \equiv \frac{m_i c^2}{8(\chi T_i) k_0^2}$ and $r_0^2 \equiv (\frac{e^2}{m_e c^2})^2$ and $d\underline{k}' = k'^2 \Delta\Omega dk'$

γ_k can then be simplified to

$$\gamma_k = - \frac{r_0^2 n_0 I (2\pi)^3}{\pi (\chi T_i) k_0^3} a \ell' \int_{-\infty}^{\infty} \frac{dk' |\underline{k}'-\underline{k}| e^{-a^2 (k'-k)^2 - \ell'^2 (k'-k_0)^2}}{|1+\beta^2 F|^2}$$

setting $x^2 \equiv \frac{m_i}{2\chi T_i} (\frac{\Delta\omega}{|\Delta\underline{k}|})^2$

$$= \frac{m_i c^2}{2\chi T_i} (\frac{k'-k}{2k_0})^2$$

$$= a^2 (k'-k)^2$$

and $\quad dx = adk'$

substituting in γ_k

$$\gamma_k = \frac{-r_0^2 n_0 I (2\pi)^3}{\pi (\chi T_i) k_0^3} a \ell' \int_{-\infty}^{\infty} \frac{x}{a} \frac{e^{-x^2} e^{-\ell'^2 [\frac{x}{a}+(k-k_0)]^2}}{|1+\beta^2 F|^2}$$

Integration cannot be done analytically and resort to numerical methods is necessary. With an experimental value for $\ell'^2 = 452$ cm^{-1} [48] and taking "$\beta^2 = T_e/T_i$" and "a" as parameters, the integration for γ_k as a function of Δk was done by computer.[49] The integration was performed with x taken from 1 to 4 using a incremental steps $\Delta x = 0.1$. (See Appendix II) The range of Δk was scanned from 2.5 cm^{-1} to 6.5 cm^{-1} at 0.05 cm^{-1} intervals to obtain a graph of γ_k versus Δk with "$\beta^2 = T_e/T_i$" and "a" as parameters.

● (ii) Discussion

All these graphs turned out to have multipeaks, i.e. the growth rate varied considerably over a small range of Δk. This is not realistic and is likely due to the finite Δx values for F(x); the program had real trouble taking more integration steps. The curve should be a smooth one (which will be seen in the next section using a delta laser spectrum; numerical integration with a narrow gaussian should give a similar result to analytic integration with a delta function).

However, the wavenumber shift at which the highest peak occurs showed good agreement with experimental shift. The case with $\beta^2 = T_e/T_i = 4$ and $T_i = 12$eV, i.e. a=0.528 (these conditions correspond to the zero magnetic field case of section 4.3) gives the highest peak from the numerical integration at $\Delta k = 3.65$ cm^{-1}. The equivalent wavelength shift is 65Å which is in complete agreement with experiment.

For the other case when $\beta^2 = T_e/T_i = 8$ and $T_i = 10$eV, i.e. a=0.578 (this approximately corresponds to the magnetic field

case), the highest peak occurs at $\Delta k = 4.25$ cm^{-1}, or $\Delta\lambda = 76\text{Å}$, in good agreement with the experimental value of 72Å.

In view of the numerical uncertainties plus the fact that the laser spectral width is small compared to the observed shifts, it is simpler to assume a monochromatic beam which permits analytical integration.

(2) Delta Function Laser Spectrum

(i) γ_k^- Evaluation via Analytical Method

If one therefore takes the spectrum of the incident waves to be essentially monochromatic, in the random phase approximation the photon density can be written as

$$N_{k'} = \frac{(2\pi)^3 I}{\hbar\omega_0 c} \delta(\underline{k}' - \underline{k}_0)$$

with this $N_{k'}$ in (19)

$$\gamma_k = -\frac{e^4}{m_e^2 c^2} \frac{\hbar n_0}{\chi T_i} \sqrt{\frac{m_i}{2\pi\chi T_i}} (2\pi)^3 \int_{-\infty}^{\infty} \frac{I}{\hbar\omega_0 c} \frac{\Delta\omega}{|\Delta\underline{k}|}$$

$$\times \frac{\delta(\underline{k}' - \underline{k}_0)}{k_0^2} \frac{e^{-\frac{m_i}{2\chi T_i}\left(\frac{\Delta\omega}{|\Delta\underline{k}|}\right)^2}}{|1+\beta^2 F(x)|^2} d\underline{k}'$$

which can be integrated to give

$$\gamma_k = -\frac{e^4}{m_e^2 c^2}\frac{n_0}{\chi T_i}\frac{I}{\omega_0 c}(2\pi)^3 \sqrt{\frac{m_i}{2\pi\chi T_i}}\frac{(\omega-\omega_0)}{|\underline{k}-\underline{k}_0|} \frac{e^{-\frac{m_i}{2\chi T_i}\frac{(\omega-\omega_0)^2}{|\underline{k}-\underline{k}_0|^2}}}{|1+\beta^2 F(x)|^2}$$

$$= -\left(\frac{e^2}{m_e c^2}\right)^2 \frac{n_0}{k_0^3}\frac{I(2\pi)^3}{\chi T_i \sqrt{\pi}}\cdot\frac{xe^{-x^2}}{|1+\beta^2 F(x)|^2}$$

$$= -(2\pi)^3 \frac{r_0^2 I n_0}{k_0^3 \chi T_i}\frac{x\Gamma_\beta(x)}{\sqrt{\pi}} \tag{20}$$

where $x^2 \equiv (\frac{m_i}{2\chi T_i})(\frac{\omega-\omega_0}{|\underline{k}-\underline{k}_0|})^2$ as before and Γ_β is given by equation (18).

Values of $\frac{x\Gamma_\beta(x)}{\sqrt{\pi}}$ were calculated by an APL computer program (Appendix II) with x ranging from 0 to 3.0 at 0.1 intervals for varying β values, $\beta=\sqrt{T_e/T_i}$. Results are shown in Fig. 22. As β increases, linear Landau damping decreases and a sharper ion wave resonance results. Evidently damping is a sensitive function of the ratio $T_e/T_i=\beta^2$.

(ii) Discussion

For $\beta=\sqrt{T_e/T_i}=2$ (corresponding to the zero magnetic field case) curve "d" in Fig. 22 shows the resonance occurs as $x\simeq 2$ where $\frac{x\Gamma_\beta(x)}{\sqrt{\pi}}=0.215$. Hence from (20)

$$x = \sqrt{\dfrac{m_i}{2XT_i}} \; \dfrac{(\omega - \omega_0)}{|\underline{k} - \underline{k}_0|}$$

$$\dfrac{x\,\Gamma_\beta(x)}{\sqrt{\pi}}$$

$\sqrt{T_e/T_i}$

a 1.00
b 1.50
c 1.75
d 2.00
e 2.25
f 2.50
g 2.75
h 3.00
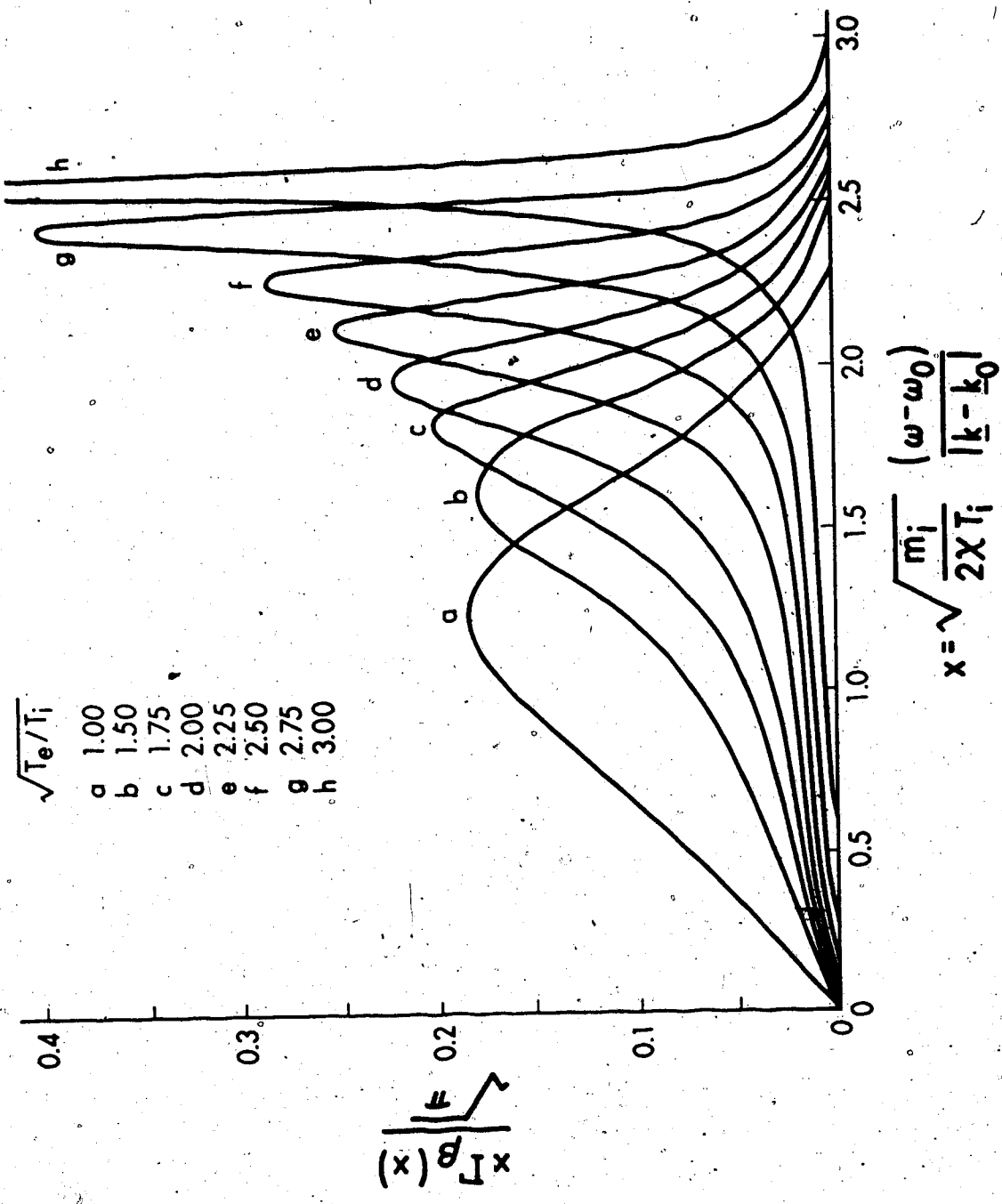
Fig. 22 Computor Plot of Stimulated Brillouin Backscattering Growth Rate Y_k

For Different T_e/T_i Ratios Based on Random Phase Theory

$$\gamma_k = \frac{(2\pi)^3 (2.83 \times 10^{-13})^2 (4 \times 10^{17})(10^{-18})}{(6000)^3 (10 \times 1.6 \times 10^{-12})} \times 0.215$$

$$= 2.3 \times 0.215 \times 10^{12}$$

$$\approx 5 \times 10^{11} \text{ sec}^{-1}$$

for our experimental conditions.

This calculated value and the experimental one of 5.93×10^{11} sec^{-1} show good agreement. Moreover, the value of x, or equivalently wavelength shift, where γ is maximum shows excellent agreement with experiment as discussed earlier.

4.7 Threshold Condition and Growth Rate Based on Wave-Concept

(1) Threshold Condition

Before the threshold and growth rate conditions shown in section 2.1(2)-c are discussed with respect to this experiment, the two damping mechanisms which may inhibit backscatter should be examined.

It was mentioned before that both collisions and Landau damping can prevent stimulated backscattering. With plasma density = 4×10^{17} cm^{-3}, $T_e = 74$ev, $\ell n\Lambda = 10$ the electron ion collision frequency is

$$\nu_{ei} = \frac{e^4 n \ell n\Lambda}{32\sqrt{2\pi} \, \epsilon_0^2 m_e^{1/2} (\chi T_e)^{3/2}}$$

$$\approx 1.5 \times 10^{-6} \frac{n \ell n\Lambda}{(T_e)^{3/2}}$$

$$= 9.4 \times 10^9 \text{ sec}^{-1}$$

and the ion-ion collision frequency is

$$\nu_{ii} = \sqrt{\frac{m_e}{m_i}} \; \nu_{ei} (\frac{T_e}{T_i})^{3/2} \times \sqrt{2}$$

$$= 4.9 \times 10^9 \text{sec}^{-1} \times \sqrt{2} = 7 \times 10^9 \text{sec}^{-1} .$$

For these experimental conditions with finite T_e/T_i Landau damping is not negligible. In fact from Fig. 22, γ_L is of order $\frac{1}{10}$ to $\frac{1}{4}$ of the frequency shift, which for $\omega_i \approx 10^{11} \text{sec}^{-1}$ implies $\gamma_L \approx 10^{10}$ to $3 \times 10^{10} \text{sec}^{-1}$ depending on T_e/T_i. Thus collisions are not negligible in comparison, though Landau damping is stronger. The experimental damping rate for no magnetic field is $\gamma_i \approx 3.5 \times 10^{10} \text{sec}^{-1}$.

Now for $I = 10^{11} \text{watts/cm}^2$, $E^2 = \frac{8\pi I}{c}$ gives

$$E = \sqrt{\frac{8\pi I}{c}} .$$

Also $\omega_{pi} = 8.3 \times 10^{11} \text{sec}^{-1}$, $T_e = 74 eV$, $n = 4 \times 10^{17} \text{cm}^{-3}$ whereby for

$$v_0 = \frac{eE}{m\omega_0} = 272\sqrt{I}$$

$$= 8.6 \times 10^7 \text{cm/sec}$$

$$v_e = \sqrt{\frac{\chi T_e}{m_e}} = 3.6 \times 10^8 \text{cm/sec}$$

the left-hand side of Equation (5) $(\frac{v_0}{v_e})^2 = 0.057$

and the right hand side of Equation (5) $\frac{\gamma_i \nu_{ei}}{\omega_i \omega_0} = 8(\frac{1}{4})(\frac{1.2 \times 10^{10}}{1.78 \times 10^{14}})$

$$= 1.3 \times 10^{-4} \text{sec}^{-1} .$$

Hence, the threshold condition $(\frac{v_0}{v_e}) >> \frac{8\gamma_i}{\omega_i} \frac{v_{ei}}{\omega_0}$

is easily satisfied.

(2) γ predicted by Wave Theory

From wave theory γ_0 is given by Equation (6)

$$\gamma_0 = \frac{1}{2} \frac{v_0}{c} (\frac{\omega_0}{\omega_i})^{\frac{1}{2}} \omega_{pi}$$

$$= \frac{1}{2} \frac{8.6 \times 10^7}{3 \times 10^{10}} (\frac{1.78 \times 10^{14}}{1.2 \times 10^{11}})^{\frac{1}{2}} (8.3 \times 10^{11})$$

$$= 4.6 \times 10^{10} sec^{-1}$$

which is within a factor of two of the experimental value.
It is interesting to note that experimental interpretation
of growth for a finite length plasma which varies exponentially
with

$$2\frac{\gamma_0^2 \ell}{\gamma_i c} \sim \frac{\gamma_0^2 n_0 I \ell}{k_0^3}$$

shows the same parametric dependence on density, intensity,
wavelength and plasma length as does the random phase predic-
tion. Thus experimentally only magnitudes could possibly
be used to distinguish between these interpretations. For
our experimental conditions it would seem that Tsytovich's
theory provides closer agreement.

(3) e-foldings

Since the plasma column is of finite length, equation
(6) gives

$$\gamma_0 \simeq \frac{1}{2} \frac{v_0}{c} \left(\frac{\omega_0}{\omega_i}\right)^{\frac{1}{2}} \omega_{pi}$$

$$= 4.6 \times 10^{10} \sec^{-1}$$

whereby (7) gives

$$\frac{\gamma_0 \ell}{\sqrt{cc_s}} = \frac{4.6 \times 10^{10} \times 0.44}{(3 \times 10^{10} \times 10^7)^{\frac{1}{2}}}$$

$$\simeq 37 > 1$$

which satisfies the finite length growth condition. In addition,

$$\gamma_T = [(3 \times 10^{10}) \frac{(1.2 \times 10^{10})}{2}]^{\frac{1}{2}} \sqrt{0.04}$$

$$= 2.7 \times 10^9 \sec^{-1}$$

whereby growth exceeding threshold $\gamma_0 > \gamma_T$ is satisfied.

Finally

$$\gamma_c \simeq \frac{1}{2}(3 \times 10^{10})(3 \times 10^3)^{\frac{1}{2}}$$

$$= 2 \times 10^{11} \sec^{-1}$$

for which $\gamma_0 < \gamma_c$ implies strong damping whereby no absolute instability can develop but considerable growth can occur if a sufficient number of e-foldings occur, i.e.

$$\frac{\gamma_0^2 \ell}{c \gamma_i} = 8.7 > 1$$

In fact, using the experimental values for γ_0 and γ_i, this condition is easily satisfied.
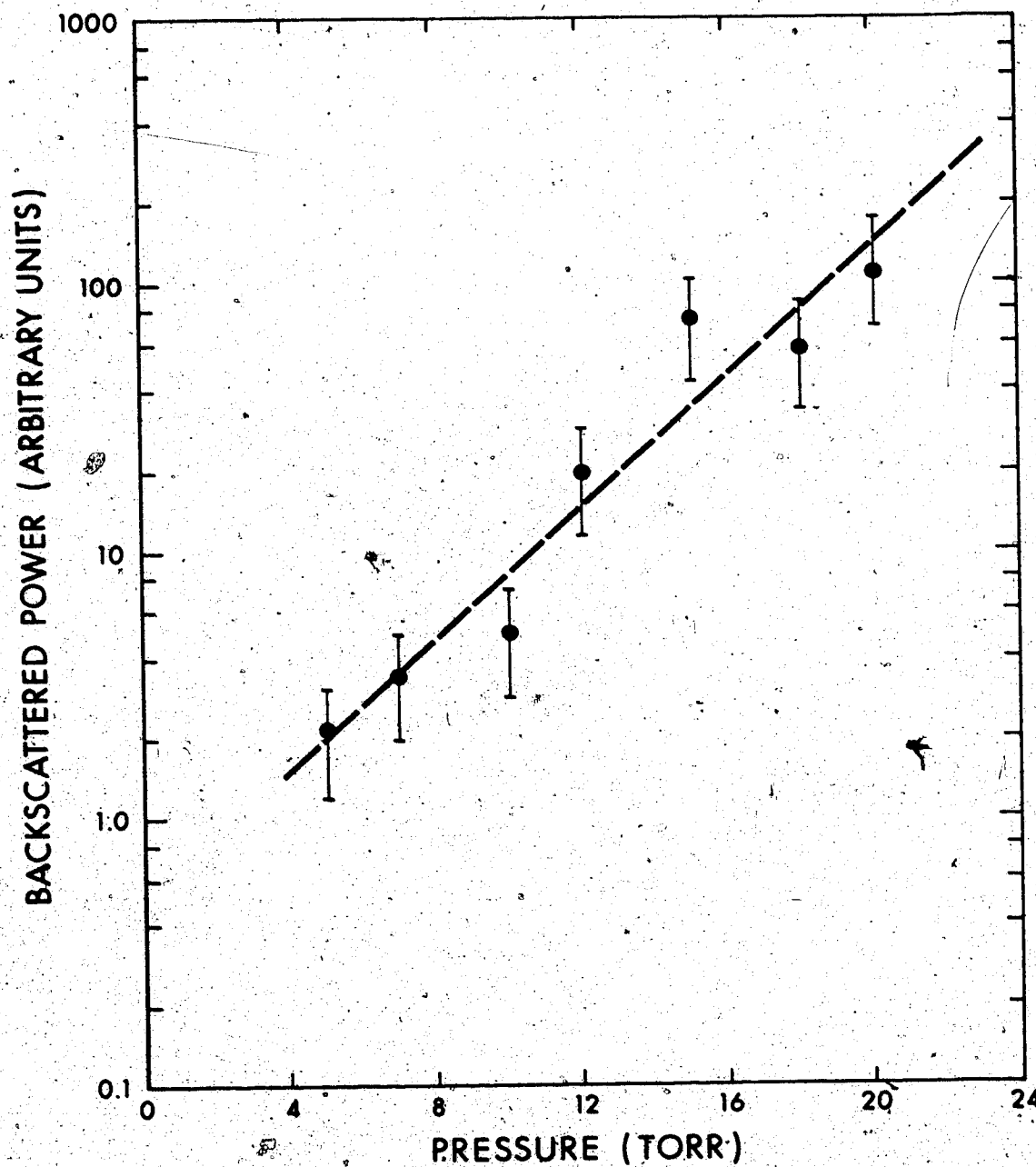
Fig. 23   Backscattered Power Versus Initial Hydrogen
Pressure in Plasma Cell for Constant Laser
Intensity

4.8 Pressure Dependence

With laser power unattenuated and hydrogen backfilled from 4 to 20 torr, the backscattered power as a function of hydrogen pressure was measured and is shown in Fig. 23. The backscattered power is clearly varying exponentially, though the slope of the line is approximately 20% less than that in Fig. 21. This is within the uncertainty in slope determination of Fig. 21 (approximately 30%) and so cannot be considered significant.

This result can be interpreted as a varying interaction length effect. Since the plasma rapidly expands radially, the density quickly reaches an asymptotic value at about 10 nsec and for times greater than 20 nsec it can be regarded as constant. On the other hand, streak photos obtained for different hydrogen pressures show a linear relationship between axial breakdown velocity and pressure. For pressures P=5,10,15,18,20 Torr, the corresponding breakdown velocities are $(0.8,1.4,2.0,2.2,2.4)\times10^7$ cm/sec. Thus, since $\ell = vt$, for a fixed time $\ell \propto P$ and one can conclude the growth in back-scattering should show an exponential variation with pressure as is observed.

CHAPTER V

DISCUSSION

Stimulated Brillouin backscattering has been observed in both underdense hydrogen and helium plasma. Clearly resolved spectral shifts were observed from non-magnetically confined plasma and magnetically confined plasma permitting backscattering from plasma with different T_e/T_i ratios. Self-consistent results are found for electron and ion temperatures which agree with hydrodynamic predictions and the theoretical predictions of ion-acoustic wave scattering from random phase waves. Experimentally γ_k was found to be 5.9×10^{11} sec^{-1}; theoretically it was calculated to be 5×10^{11} sec^{-1}. The intensity dependence of the backscattered power also agreed with random phase predictions.

The measured redshift for B=0 was 65 Å and the spectrum had a FWHM of 21 Å while for B=110 K Gauss, the ion acoustic shift was 72 Å and FWHM 35 Å. This broader width is an unexpected result. According to the theory, the linewidth narrows as $\beta=\sqrt{T_e/T_i}$ increases, because for a higher T_e/T_i ratio, linear Landau damping decreases. Possibilities for increased spectral broadening in the magnetically confined case may be due to (i) increased turbulence in plasma during laser plasma interaction (ii) nonlinear Landau damping and (iii) reduced ion-acoustic wave amplitude due to higher thermal energy content. This is only conjecture and the true physics to account for such broadening requires

75

further experiment. Observation of the ion-acoustic shift
and broadening for higher intensity laser radiation as well
as saturation of backscattered power would be useful.
This experiment shows that for the described laboratory con-
ditions, only 0.2% of power is backscattered.

Threshold conditions are found to be easily exceeded in
this experiment. Detailed discussion for the magnetic field
case was presented; similar results hold true for the non-
magnetically confined plasma.

The spectral shift of 30 Å from helium plasma showed
the inverse square root relationship of mass of ion with
wavelength shift, thus confirming the presence of ion-
acoustic waves as responsible for stimulated Brillouin
backscattering.

BIBLIOGRAPHY

1. J.M. Dawson, R.E. Kidder and A. Herzberg. AEC Research and Development Report. MATT 782, Princeton, (1971).

2. K. Nishikawa. J. Phys. Soc. Japan. 24 (1968) 916.

3. K. Nishikawa. J. Phys. Soc. Japan. 24 (1968) 1152.

4. A.A. Galeev and R.Z. Sagdeev. Nuclear Fusion. 13 (1973) 603.

5. M.N. Rosenbluth. Phys. Rev. Lett. 29 (1972) 565.

6. R. Stenzel and A.Y. Wong. Phys. Rev. Lett. 28 (1972) 274.

7. R. Chang, M. Porkolab and B. Greek. Phys. Rev. Lett. 28 (1972) 206.

8. Ref. 4.

9. D.F. Dubois, Laser Interaction and Related Plasma Phenomena. 3A (1974) 267, Plenum Press, New York.

10. Ref. 1.

11. F.W. Perkins and J. Flick, Phys. Fluid. 14 (1971) 1012.

12. M.N. Rosenbluth, R.B. White and C.S. Liu, Phys. Rev. Lett. 31 (1973) 1190.

13. A.A. Galeev, G. Laval, T. O'Neil, R. and R. Sagdeev. JETP Lett. 17 (1973) 35.

14. D.W. Forslund, J.M. Kindel, E.L. Lindman. Phys. Rev. Lett. 30 (1973) 739.

15. C.S. Liu, M.N. Rosenbluth and White. Phys. Rev. Lett. 31 (1973) 697.

16. D. Pesme, G. Laval, R. Pellat. Phys. Rev. Lett. 31 (1973) 203.

17. P.K. Shukla, M.Y. Yu, K.H. Spatschek. Phys. Fluid 18 (1975) 265.

18. L.M. Goldman, J. Soures and M.J. Lubin. Phys. Rev. Lett. 31 (1973) 19.

19. J.J. Turechek, F.F. Chen and N.C. Luhmann. Jr. Bull. Amer. Phys. Soc. 19 (1974) 919.

20. R. Massey, K. Berggren and Z.A. Pietrzyk. Proc. of the Fifth Annual Anomalous Absorption Conference at UCLA, C4, April (1975).

21. H.J. Schwarz and H. Hora (editors). Laser Interaction and Related Plasma Phenomenon. Vol. 3A, Plenum Press, New York.

22. Ref. 2.

23. C.N. Lashmore-Davies. Plasma Phys. 17 (1975) 281.

24. Ref. 23.

25. F.F. Chen. Introduction to Plasma Physics. Plenum Press, 1974, New York.

26. J.A. Fejer. Can. J. Phys. 38 (1960) 1114.

27. J. Sheffield. Plasma Scattering of Electromagnetic Radiation. Academic Press, 1975, New York.

28. A.G. Litvak, V. Yu. Trakhtengerts. Sov. Phys. JETP 33 (1971) 921.

29. V.N. Tsytovich. Sov. Phys. USPEKHI 9 (1966) 805.

30. V.N. Tsytovich. Nonlinear Effects in Plasma. Plenum Press, 1970, New York.

31. E.E. Salpeter. Phys. Rev. 120 (1960) 1528.

32. N.H. Burnett and A.A. Offenberger. J. Appl. Phys. 44 (1973) 3617.

33. O.P. Judd. Appl. Phys. Lett. 22 (1973) 95.

34. A.K. Levine and A.J. Demaria (editors). Lasers, A series of Advances. Dekker Press, (1971), New York.

35. M.C. Richardson, A.J. Alcock, K. Leopold and P. Burtyn. IEEE J. Quant. Electr. QE9 (1973) 236.

36. H. Seguin and J. Tulip. Appl. Phys. Lett. 21 (1972) 414.

37. Ref. 32.

38. From Discussion within U. of Alberta Plasma Group, with A.A. Offenberger, D.F. Way-Nee and B.H. Hadley.

39. A.A. Offenberger and N.H. Burnett. J. Appl. Phys. 43 (1972) 4977.

40.   A.A. Offenberger and N.H. Burnett. J. Appl. Phys. 45 (1974) 623.

41.   G. Vlases. C.A.P. Plasma and Fusion Summer School at Banff. (1975) unpublished.

42.   A.A. Offenberger, M.R. Cervenan, A.M. Yam and A.W. Pasternak. Private discussion (unpublished).

43.   A.A. Offenberger, P.R. Smy and N.H. Burnett. Rev. Sci. Instrum. 46 (1975) 317.

44.   A.M. Robinson, M. Nohr. Rev. Sci. Inst. 45 (1974) 1605.

45.   F.A. Jenkins, H.E. White. Fundamental of Optics. McGraw-Hill, 1957.

46.   N.H. Burnett, A.A. Offenberger. J. Appl. Phys. 45 (1974) 2155.

47.   B.D. Fried and S.D. Conte. The Plasma Dispersion Function. Academic Press, New York (1961).

48.   A.A. Offenberger, R.D. Kerr. Phys. Lett. 37A (1971) 435.

49.   APL, University of Alberta Computing Service.
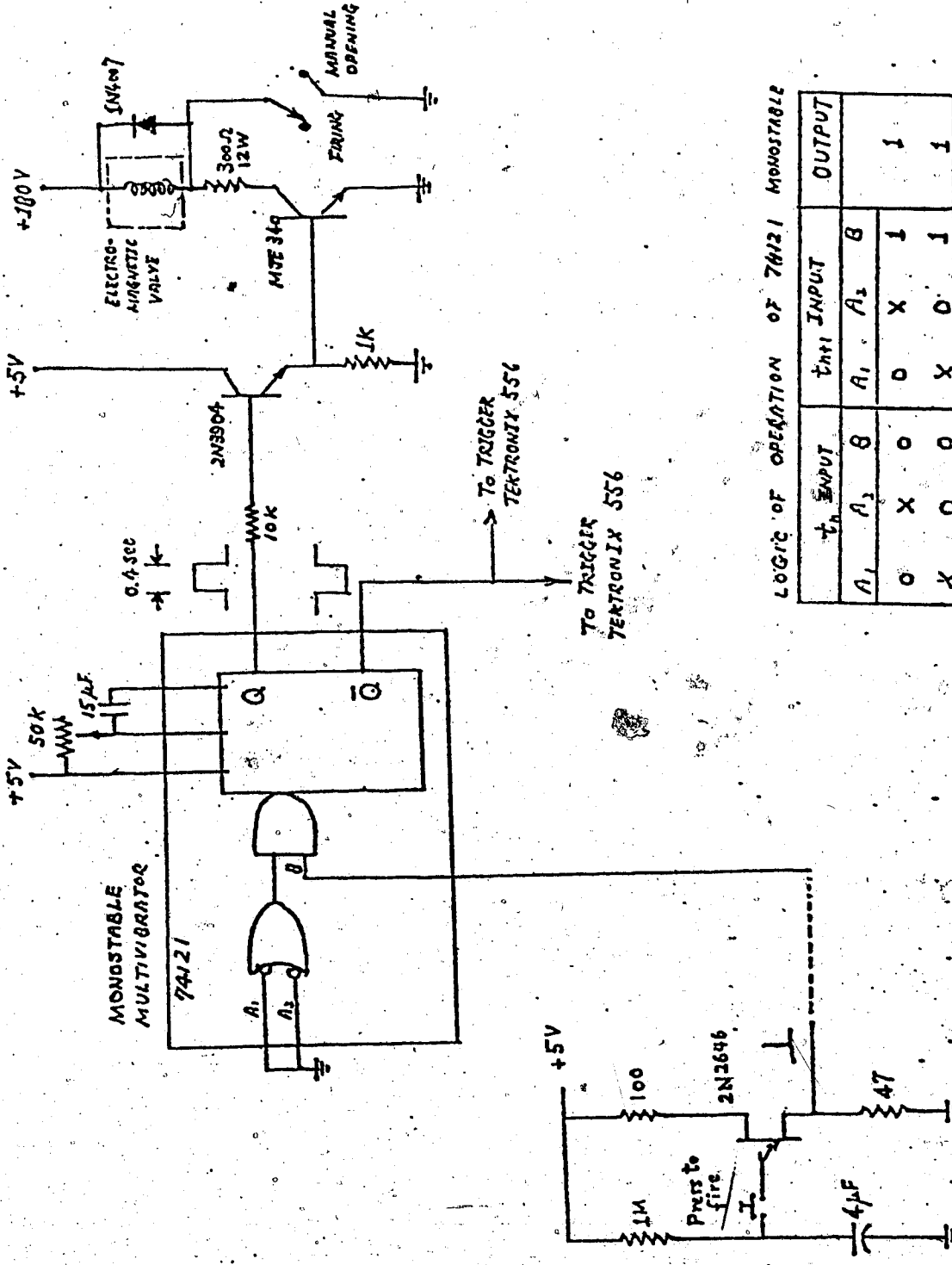
LOGIC OF OPERATION OF 74121 MONOSTABLE

t_n INPUT		t_{n+1} INPUT		OUTPUT
A_1	B	A_1	A_2	B
0	0	0	X	1
X	0	X	0	1

X = don't care

APPENDIX II

COMPUTER PROGRAMS

The APL ($\underline{A}$ $\underline{P}$rogramming $\underline{L}$anguage) programs used to evaluate γ_k are described below.

(1) Using Gaussian Laser Spectrum

Aim: (i) A function "GRTH" was designed to evaluate numerically, for a particular $\Delta k \equiv k - k_0$,

$$D = \int_1^4 \frac{xe^{-x^2} e^{-\ell'^2 [\frac{x}{a}+\Delta k]^2}}{a|1+\beta^2 F(x)|^2} dx$$

for finite ███████ nd "β^2".

(ii) Assuming array $\Delta k = \Delta k(1) \; \Delta k(2) \; \dots \; \Delta k(N)$

array $D = D(1) \; D(2) \; \dots \; D(N)$

program plots D Vs Δk.

Imput: array Y = string of x (0.1 interval from 1 to 4),

β^2, a, 0 (zero)

array Z = Re(Z), Im(Z) values corresponding to each

x, from "Plasma Dispersion Function

Table" (Ref. 47)

Flowchart: Function [Y GRTH Z]

```
┌─────────────────────┐
│  Generate string of │
│         Δk          │
└─────────────────────┘
           │
           ▼
┌─────────────────────┐
│  Find N ← number of │
│         Δk          │
└─────────────────────┘
           │
           ▼
```

```
        L ← 1
No  ◄── Is L ≤ N? ──► Yes
        L ← L + 1
```

┌──────────────────────────┐
│ Plot D Vs Δk   │
│ using Function   │
│ "PLOT"   │
└──────────────────────────┘

┌──┐
│ Numerically integrate   │
│   │
│ $D(L) = \int_1^4 \frac{B}{A}\,dx$ │
│   │
│ where $A \leftarrow |1+\beta^2 F(x)|$ │
│   │
│ $B \leftarrow \frac{x}{a} e^{-x^2} e^{-\ell^2[\frac{x}{a}+\Delta k(L)]}$ │
└──┘

┌──────────────────────┐
│ Form a 2 by L   │
│ matrix: │
│ $[\frac{\Delta k(L)}{D(L)}]$ │
└──────────────────────┘
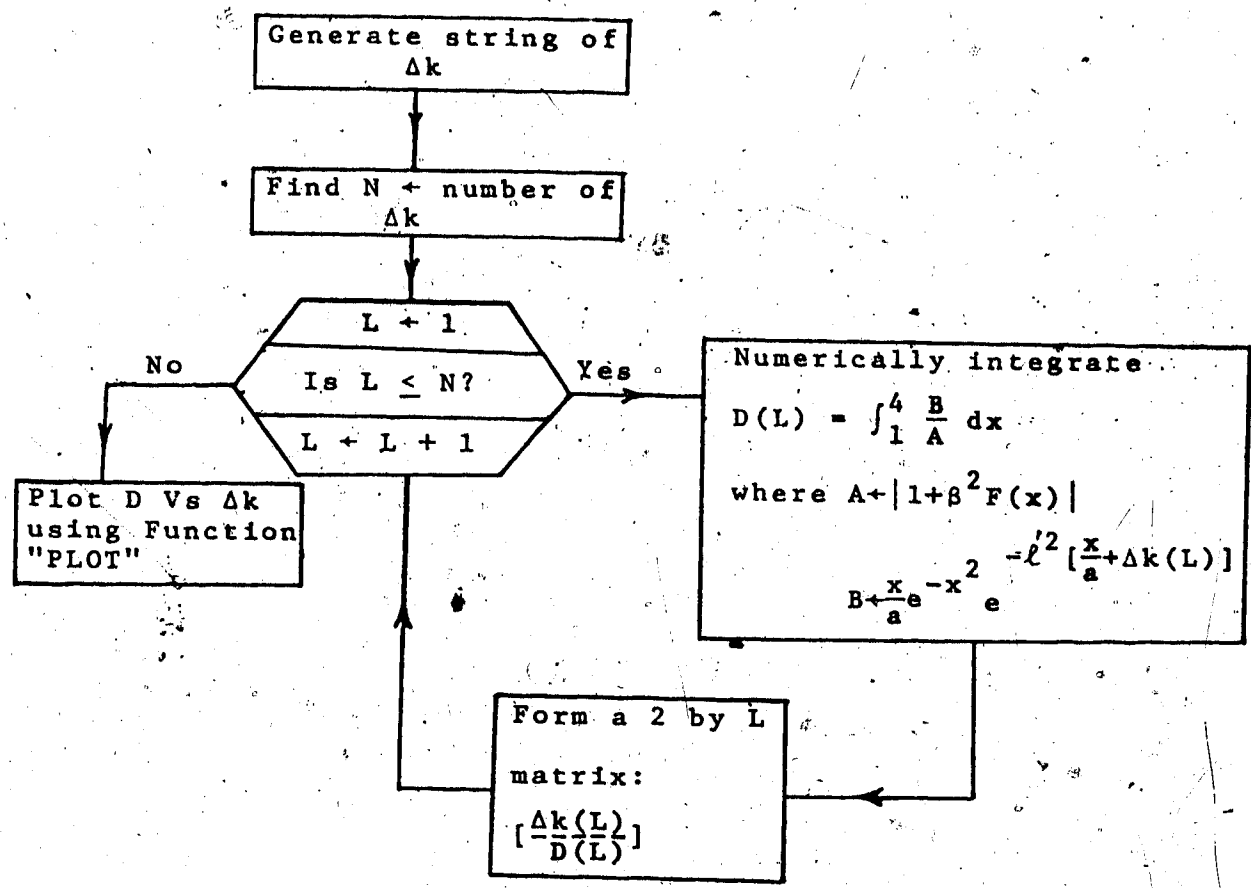
Note: Function "PLOT" can be hauled out from U. of A. APL

Public Library; see "PROGRAM DOCUMENTATION" section.

(2) <u>Using a Delta Function Laser Spectrum</u>
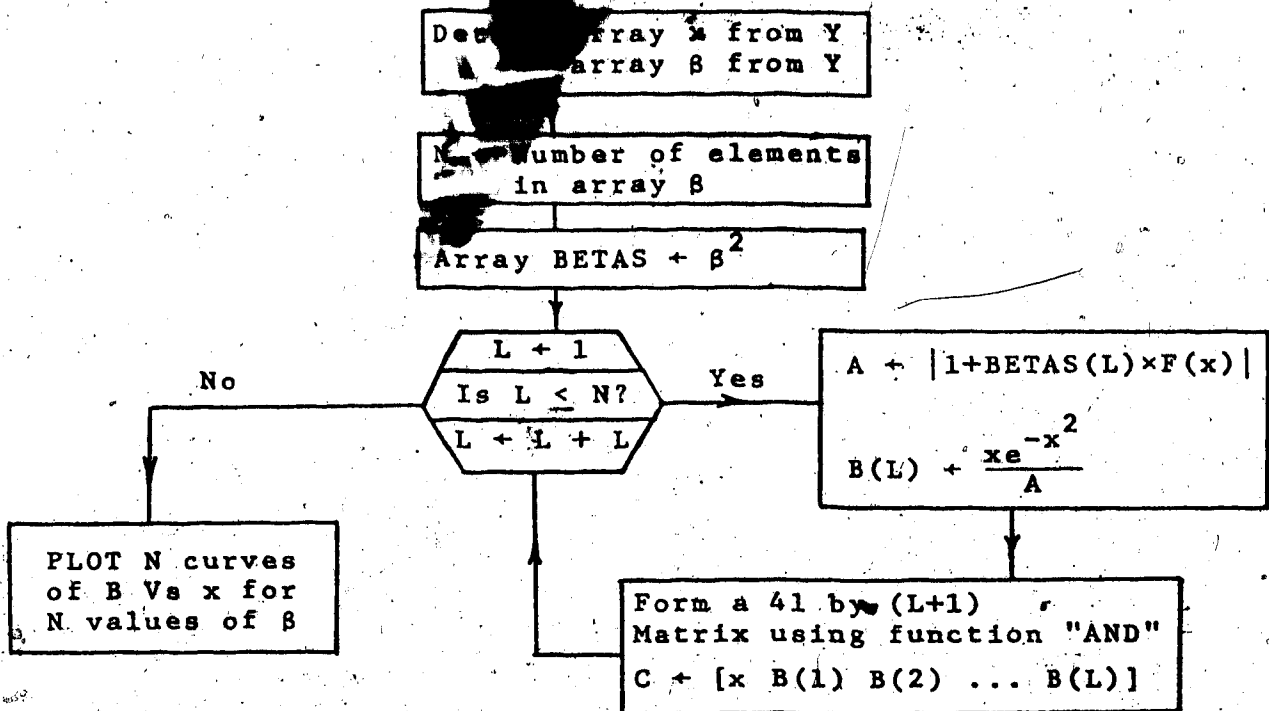
Aim: (i) A function "FN" was designed to evaluate

$$B = \frac{xe^{-x^2}}{|1+\beta^2 F(x)|^2} \cdot \frac{1}{\sqrt{\pi}} = \frac{x\Gamma_\beta(x)}{\sqrt{\pi}}$$

(ii) To plot $\frac{x\Gamma_\beta(x)}{\sqrt{\pi}}$ Vs x for different values of β

Input: array Y = values of x(0.1 interval from 0 to 4),

different values of β.

array Z = Re(z), Im(z). values corresponding to each

x, again from Table of Ref. 47

Flowchart: Function [Y FN

Det   ray   from Y
   array β from Y

N   umber of elements
   in array β

Array BETAS ← $β^2$

L ← 1
Is L ≤ N?
L ← L + L

No   Yes

A ← |1+BETAS(L)×F(x)|

$$B(L) ← \frac{xe^{-x^2}}{A}$$

PLOT N curves
of B Vs x for
N values of β

Form a 41 by (L+1)
Matrix using function "AND"
C ← [x B(1) B(2) ... B(L)]

(3) Program Documentation:

The function "GRTH" and "FN" are printed out in the
following pages. Note that function "AND" and "PLOT" are
stored under "PLOTFORMAT" of Library 1 in University of
Alberta APL Public Library. (See APL Public Library Do-
cumentation by E.G. Armitage, U. of A. Computing Services
reference manual, 1972.)

```
        )COPY YANGRDS
 SAVED  12.16.34 07/10/75
        ∇GRTH[□]∇
   ∇  SBS←Y GRTH Z;REZ;IMZ;A;B;C;D;E;K;N;T;O;N
[1]     'A-M-S YAM,JULY 16,1975.'
[2]     'APL-TO--FIND-GROWTH-RATE-OF-STIMULATED-BRILLOUIN-BACKSCATTERING÷FOR-ONE-ΔX'
[3]     K←(49+(ι130))×0.05
[4]     L←1
[5]     D←ι0
[6]     N←(ρZ)÷2
[7]     REZ←N↑Z
[8]     IMZ←N↓Z
[9]     X←N↑Y
[10]    →2Λ×ι((ρX)÷1)=L
[11]    Y[N+3]←K[L]
[12]    L←L+1
[13]    A←((1+((1+X×REZ)×Y[N+1])÷2)+((Y[N+1]×X×IMZ)÷2)
[14]    B←(X÷(Y[N+2]))×(÷(-((X×2)+(((X÷(Y[N+2]))-Y[N+3])÷2)×÷52)))
[15]    C←N±A
[16]    W←(2,(ρX))ρ(X,C)
[17]    →19×ι2=ρρW
[18]    →0,ρ⎕←'REQUIRE DATA POINTS MATRIX ARGUMENT'
[19]    T←W[1;]
[20]    K←¯1 0 ÷W
[21]    →25×ι(2≤ρT)ΛΛ/T=R←1+T←1+T-¯1ΦT
[22]    E←(0 1 +W+¯1ΦW)+.×T÷2
[23]    D←D,E
[24]    →10
[25]    E←(N÷6)×I/÷.×2,(((¯1-O-ρT)ρ 8 4),(1+O)ρ 2 0 +3×O÷2|ρT
[26]    D←D,E
[27]    →10
[28]    SBS←D
[29]    ¯3+Y
   ∇
[30]
```

```apl
      ∇FN[□]
    ∇ Y FN Z;A;B;C;N;REZ;IMZ;RPT;L;BETAS;L
[1]   RPI←1÷(3.14159*0.5)
[2]   L←1
[3]   N←(ρZ)÷2
[4]   REZ←N↑Z
[5]   IMZ←N↓Z
[6]   X←N+Y
[7]   BETAS←-(N+Y)÷2
[8]   →18×ι((ρBETAS)+1)=L
[9]   Y[N+1]←BETAS[L]
[10]  L←L+1
[11]  A←((1+((1+X×REZ)×Y[N+1]))*2)+((Y[N+1]×X×IMZ)*2)
[12]  B←((X×(*(-(X*2))))×RPI)+A
[13]  →16×ιL=2
[14]  C←C AND B
[15]  →8
[16]  C←X AND B
[17]  →0
[18]  'A M S YAM JULY 22,1975.'
[19]  'APL TO FIND GROWTH RATE OF STIMULATED BRILLOUIN BACKSCATTERING'
[20]  120 120 PLOT C
[21]  N+Y
[22]  'PLOTTING CODES O+∘∇+□×∆ CORRESPONDS TO DIFFERENT BETASQUARES'
[23]  C
    ∇
```